

## Chapter 2

# Development of Microsystems Multi Physics Investigation Methods

**Abstract** The theoretical and experimental methods for the investigation of microsystems multi physic processes are presented. The FEM method for the analysis of MEMS in digital environment in combination with experimental data from holographic interferometry is developed. Numerical–experimental method for evaluation of geometrical parameters and their usage for characterization of microstructures is presented. In order to optimise hot imprint method in polycarbonate, an elasto-plastic material model for simulation of microstructures hot imprint method is developed.

### 2.1 Application of Time Averaged Holography for Micro-Electro-Mechanical System Performing Non-linear Oscillations

To perform the analysis of the links of MEMS systems time average laser holography [1] may be applied. Time average laser holography is a non-destructive full field technique, which may be used of investigation and analysis of dynamics of vibrating amplitudes and static displacements of deformable surface of MEMS components [2]. In combination with optical and digital holography numerous numerical methods [3] used for interpretation of patterns of fringes of holographic interferograms of analysed MEMS. Sometimes because of nonlinearities of MEMS links interpretation and analysis of holographic interferogram needs additional numerical investigations. An example of synergy of this methodology is presented in this chapter. The sequency of manufacturing technology of a micro-electromechanical switch used for the analysis follows.

The manufacturing of the MEM switch begins with the patterning and reactive ion etching of silicon using  $\text{SF}_6/\text{N}_2$  gas chemistry in the cantilever support area fabricating microstructures to increase the cantilever bond strength either durability of the device. After treatment of the substrate in the  $\text{O}_2/\text{N}_2$  gases mixture plasma chrome layer of about 30 nm thickness and gold layer of about 200 nm thickness were deposited. Patterning of the source, gate and drain electrodes were performed

using lift-off lithography. Electron beam evaporation was performed to deposit a sacrificial copper layer with thickness of about 3000 nm. Copper layer covered the whole area of the substrate. Patterning of the copper layer was performed in two steps. First of all, the copper layer was partially etched (etchant:  $\text{H}_2\text{SO}_4:\text{CrO}_3:\text{H}_2\text{O}$ ) to define the contact tips for the cantilever and etching duration directly determined the spacing between tip's top and drain electrode. Next, the copper layer was etched away to uncover the source cantilever support area. The next step was photo resist patterning on the top of the sacrificial layer to define the mask for the cantilever sector and lift-off lithography of the evaporated gold layer with thickness of about 200 nm was performed. Afterwards, the photoresist was spun and patterned once again in the same sector and thick nickel layer was electroplated (sulfamate electrolyte:  $\text{Ni}(\text{NH}_2\text{SO}_3)_2 \cdot 4\text{H}_2\text{O}$ ) fabricating cantilever structure. Finally, the sacrificial layer was removed away using the same wet copper etchant to release the free-standing cantilever. The general view of MEMS cantilever is presented in Fig. 2.1.

The holographic interferogram of MEMS cantilever are presented in Fig. 2.2. The methodology of recording holographic interferogram is described in [4]. During registration holographic interferogram at first MEMS cantilever was excited acoustically (Fig. 2.2a). In Fig. 2.2b holographic interferogram is registered of cantilever excited by oscillating charge of the drain electrode.

The ordinary fringe counting techniques are applied for the reconstruction of the field of vibration amplitudes in case of acoustically excited cantilever because the sinusoidal periodical excitation was used and the methods for interpretation of time-average holographic interferograms are discussed well.

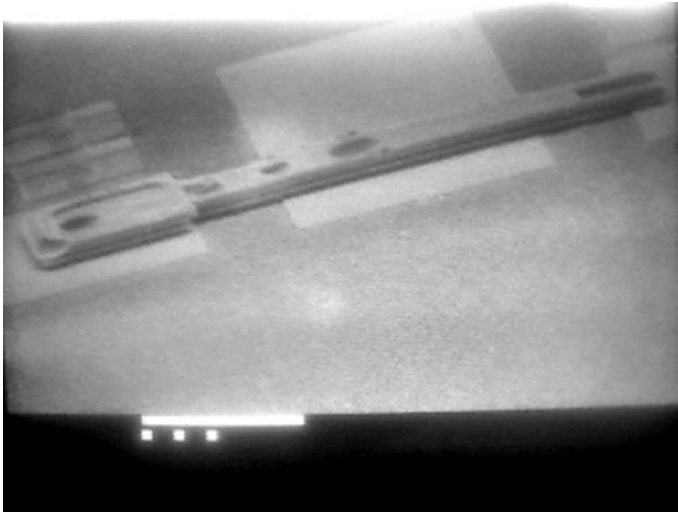


**Fig. 2.1** Microscopic photo of MEMS cantilever

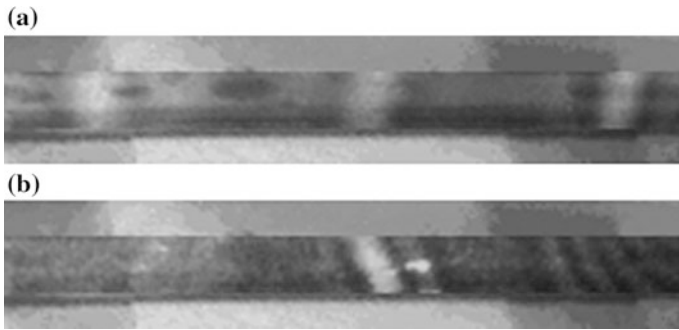


**Fig. 2.2** Holographic interferograms of cantilever: **a** holographic interferogram of cantilever acoustically excited; **b** holographic interferogram of cantilever excited by oscillating charge

The interpretation of holographic interferogram presented in Fig. 2.2b is much more complicated. The knowing the fact that cantilever excited by oscillating charge assist as to evaluate holographic interferogram taking into account the nonlinearities of vibrating surface of cantilever. Because of chaotic processes of vibrating cantilever the time exposure of recording holographic interferogram should be managed because longer exposure times produce dark images when the cantilever is excited by oscillating charge and the pattern of fringes is sensitive to exposure time and the quality of the holographic images are pure.

The interpretation of pattern of fringes in Fig. 2.2b is much more complicated—one white and several dark fringes are distributed on the surface of cantilever and it is quite difficult to understand the dynamics of the cantilever. Moreover, longer exposure times produce dark images when the cantilever is excited by oscillating charge and the pattern of fringes is sensitive to exposure time. Developing hybrid numerical–experimental models of analysed dynamical systems in this case let as to analyse generated patterns of fringes in holograms of MEMS cantilevers excited by oscillating charge originated in order to get much more characteristic about the motion of the objects.

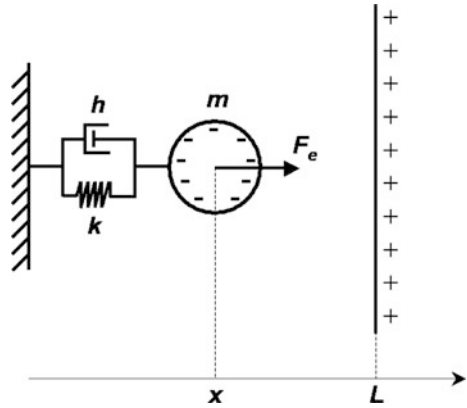
This approach when simulation of the dynamic is used as well as optical processes taking place in the analysed systems could help understanding experimental results.

### 2.1.1 *Phenomenological Model of MEMS Cantilever*

To achieve this goal in analysing complex MEMS cantilever motion the development of simple one-dimensional phenomenological model is presented in Fig. 2.3.

Governing equation of motion of the system presented in Fig. 2.3 takes the following form:

**Fig. 2.3** One degree of freedom phenomenological model of MEMS cantilever



$$m\ddot{x} + h\dot{x} + kx = F_e(x) \quad (2.1)$$

where  $m$ ,  $h$ ,  $k$ —mass, viscous damping and stiffness coefficients;  $x$ —co-ordinate;  $F_e$ —electrostatic force; top dots denote full derivatives by time  $t$ . It is assumed that the charged contact plane is motionlessly fixed at co-ordinate  $L$  (Fig. 2.3). Mass  $m$  is negatively charged, while the charge  $Q$  of the contact plane varies harmonically in time:

$$Q = q \sin(\omega t) \quad (2.2)$$

where  $q$ —maximum charge of the contact plane;  $\omega$ —frequency of charge oscillation. Then the electrostatic force  $F_e$  acting to mass  $m$  is

$$F_e = C \frac{Q}{L - x} \quad (2.3)$$

where constant  $C$  depends from the charge of mass  $m$ , density of air, etc.

The charge of the contact plane because of harmonic oscillation provides a strongly nonlinear response. That is a result because governing equation of motion is non-linear. The non-linearity of the vibration of the mass  $m$  occur when the frequency of charge oscillation is around the natural frequency of the cantilever (Fig. 2.4). Usually the frequency of charge oscillation very rarely reaches the fundamental frequency of the MEMS cantilever only due to the fact that it is very high and the excitation frequencies are of magnitude lower than fundamental frequencies.

The developed phenomenological cantilever model is analysed when the excitation frequency is much lower than the fundamental frequency and the differential equation turns to be stiff and special care is required applying direct time marching integration techniques. First the system is integrated until the transient processes cease down. Then the attractor in phase plane  $x - \dot{x}$  is drawn. Array of attractors as shown in Fig. 2.5 is built of repetition of such procedure at different values of

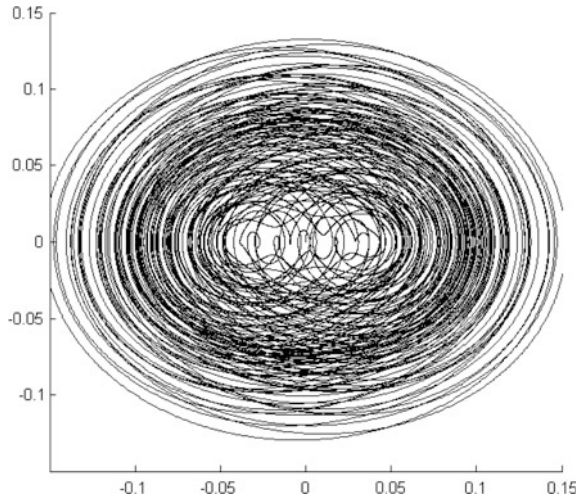


**Fig. 2.4** Chaotic motion of mass  $m$  in phase plane  $x - \dot{x}$  at  $m = 1$ ;  $k = 1$ ;  $h = 0.003$ ;  $\omega = 0.73$ ;  $q = 0.1$ ;  $L = 2$

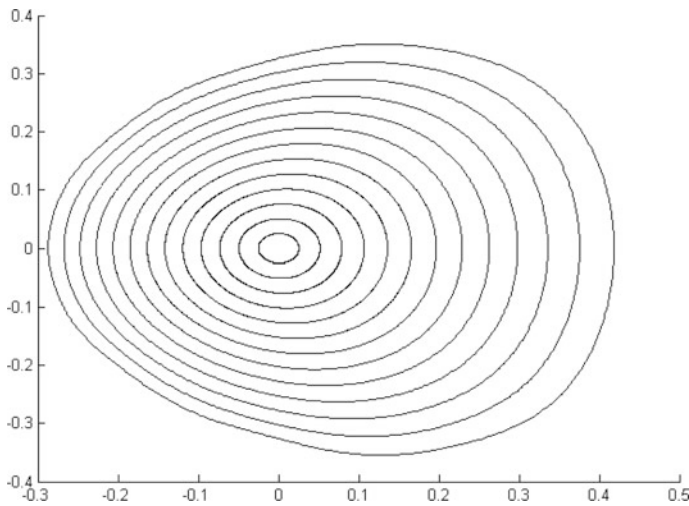


**Fig. 2.5** Stable attractors at  $m = 0.25$ ;  $k = 20$ ;  $h = 0.1$ ;  $\omega = 1$ ;  $L = 2$ ;  $q = 1, 2, \dots, 13$

maximum charge  $q$ . The motion of the mass  $m$  is almost linear at small excitation. The form of the stable attractor gradually deforms at increasing excitation what is a natural result for a non-linear system.

When we use holographic interferometry method how the experimental results could be interpreted if the analysed object would oscillate not harmonically, but as shown in Fig. 2.5.

For simplicity we deal with one-dimensional system. Then the intensity of illumination  $I$  in the hologram plane will be:

$$I = \lim_{T \rightarrow \infty} \frac{1}{T^2} \left| \int_0^T \exp\left(j \frac{2\pi}{\lambda} \zeta(t)\right) dt \right|^2 \quad (2.4)$$

where  $T$ —exposure time;  $\lambda$ —laser wavelength;  $\zeta$ —scalar time process;  $j$ —imaginary unit. When  $\zeta(t) = a \sin(\omega t + \varphi)$  where  $a$ ,  $\omega$ ,  $\varphi$ —amplitude, angular frequency and phase of oscillations, the intensity of illumination takes the form:

$$\begin{aligned} I &= \left| J_0\left(\frac{2\pi}{\lambda} a\right) \right|^2 = \lim_{T \rightarrow \infty} \frac{1}{T^2} \left( \int_0^T \cos\left(\frac{2\pi}{\lambda} a \sin(\omega t + \varphi)\right) dt \right)^2 \\ &\approx \left( \frac{1}{m} \sum_{i=1}^m \cos\left(\frac{2\pi}{\lambda} a \sin\left(\frac{2\pi}{m}(i-1)\right)\right) \right)^2 \end{aligned} \quad (2.5)$$

where  $J_0$ —zero order Bessel function of the first kind. It can be noted that  $\lim_{T \rightarrow \infty} \int_0^T \sin\left(\frac{2\pi}{\lambda} a \sin(\omega t + \varphi)\right) dt = 0$  due to evenness of the sine function, and that the angular frequency and phase have no effect to the intensity of illumination. The second approximate equality builds the ground for numerical modelling of the relationships governing the formation of interference fringes.

If  $\zeta(t)$  is not a harmonic process the intensity of illumination can be numerically reconstructed from Eq. (2.4), but the calculation is more complex than in Eq. (2.5) due to the fact the integral  $\lim_{T \rightarrow \infty} \int_0^T \sin\left(\frac{2\pi}{\lambda} \zeta(t)\right) dt$  does not converge to zero. If  $\zeta(t)$  is a periodic process and  $T_p$  is the time length if the period, the approximate numerical calculation scheme takes the following form:

$$\begin{aligned} I &\approx \left( \frac{1}{m} \sum_{i=1}^m \cos\left(\frac{2\pi}{\lambda} \zeta\left(t_0 + \frac{T_p}{m}(i-1)\right)\right) \right)^2 \\ &\quad + \left( \frac{1}{m} \sum_{i=1}^m \sin\left(\frac{2\pi}{\lambda} \zeta\left(t_0 + \frac{T_p}{m}(i-1)\right)\right) \right)^2 \end{aligned} \quad (2.6)$$

where  $t_0$ —arbitrary selected time moment. If  $\zeta(t)$  is a process characterising time history of a dynamical system setting to a stable limit cycle type attractor, time moment  $t_0$  must be selected large enough so that the transient processes are ceased. Such calculations are performed for an array of attractors shown in Fig. 2.6. One hundred separate solutions of Eq. (2.1) are analysed at intermittent values of  $q$  in the range from 0 to 13. The produced intensities of illumination are presented in Fig. 2.6 ( $x$  axis denotes 100 separate problems).

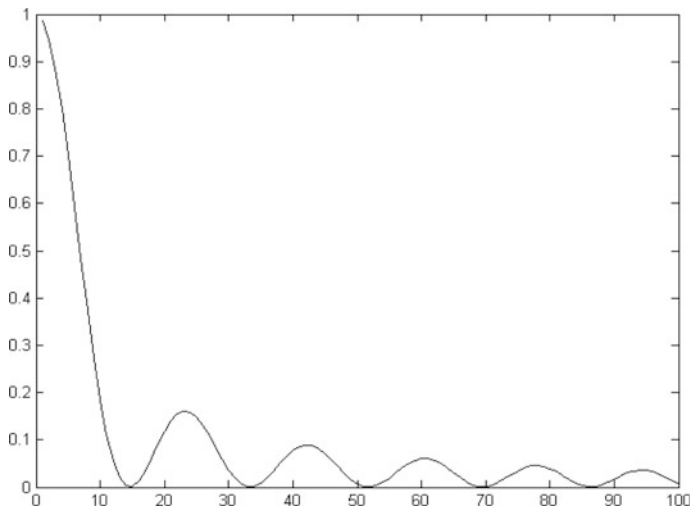


**Fig. 2.6** Relationship between intensities of illumination and parameter  $q$

Remarkable is the fact that the relationship between the intensity of illumination and parameter  $q$  holds the same character as the square of Bessel function in Eq. (2.5). In other words, the inverse problem of the reconstruction of dynamic displacements does not have a unique solution. Interference fringes can be formed when the analysed object performs harmonic vibrations. Very similar interference fringes will be formed when the object will perform non-linear periodic oscillations. Thus though time average laser holography is a very attractive technique for analysis of MEMS cantilever vibrations, the interpretation of experimentally produced interference fringes is rather complex procedure if one cannot be sure if the vibrations are harmonic. This effect is illustrated in Fig. 2.7. The presented non-linear periodic oscillation and harmonic vibration will both generate the same intensity of illumination corresponding to the centre of the sixth interference fringe. It can be noted that time average laser holography is insensitive to static shifts of harmonic oscillations. That follows from the property of Bessel function:

$$\begin{aligned}
 & \lim_{T \rightarrow \infty} \frac{1}{T^2} \left| \int_0^T \exp \left( j \frac{2\pi}{\lambda} (a \sin(\omega t + \varphi) + C) \right) dt \right|^2 \\
 &= \lim_{T \rightarrow \infty} \frac{1}{T^2} \left| \int_0^T \exp \left( j \frac{2\pi}{\lambda} (a \sin(\omega t + \varphi)) \right) dt \right|^2 = \left( J_0 \left( \frac{2\pi}{\lambda} a \right) \right)^2
 \end{aligned} \tag{2.7}$$

where  $C$ —constant. Results presented in Fig. 2.7 are remarkable not for the difference between the averages of non-linear and harmonic vibrations. Interesting is the fact that two different trajectories generate same intensity of illumination.

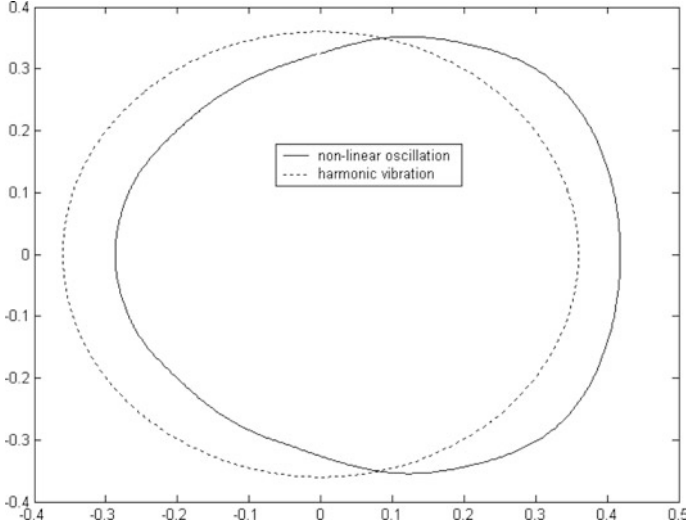


**Fig. 2.7** Two different trajectories generating same intensity of illumination

When we have chaotic oscillations the illumination of intensity can be calculated for certain stochastic time series approximating process  $\zeta(t)$ . If a time series  $\zeta_i$  is normally distributed with variance  $\sigma^2$  then, the decay of intensity of illumination can be calculated as follows:

$$\begin{aligned}
 I &\approx \lim_{m \rightarrow \infty} \left( \left( \frac{1}{m} \sum_{i=1}^m \cos\left(\frac{2\pi}{\lambda} \zeta_i\right) \right)^2 + \left( \frac{1}{m} \sum_{i=1}^m \sin\left(\frac{2\pi}{\lambda} \zeta_i\right) \right)^2 \right) \\
 &= \lim_{m \rightarrow \infty} \left( \frac{1}{m} \sum_{i=1}^m \sum_{k=0}^{+\infty} \frac{(-1)^k \left(\frac{2\pi}{\lambda} \zeta_i\right)^{2k}}{(2k)!} \right)^2 = \left( \sum_{k=0}^{+\infty} \frac{(-1)^k \left(\frac{2\pi}{\lambda}\right)^{2k}}{(2k)!} \lim_{m \rightarrow \infty} \sum_{i=1}^m \frac{(\zeta_i)^{2k}}{m} \right)^2 \\
 &= \left( \sum_{k=0}^{+\infty} \frac{(-1)^k \left(\frac{2\pi}{\lambda}\right)^{2k}}{(2k)!} \cdot (2k-1)!! \cdot \sigma^{2k} \right)^2 = \left( \sum_{k=0}^{+\infty} \frac{(-1)^k \left(\frac{2\pi}{\lambda} \sigma\right)^{2k}}{(2k)!!} \right)^2 \\
 &= \left( \sum_{k=0}^{+\infty} \frac{(-1)^k \left(\frac{2\pi}{\lambda} \sigma\right)^{2k}}{2^k k!} \right)^2 = \left( \sum_{k=0}^{+\infty} \frac{(-1)^k}{k!} \left( \frac{1}{2} \left(\frac{2\pi}{\lambda} \sigma\right)^2 \right)^k \right)^2 = \exp^2 \left( -\frac{1}{2} \left(\frac{2\pi}{\lambda} \sigma\right)^2 \right)
 \end{aligned} \tag{2.8}$$

The following identities are used in Eq. (2.8). If  $\zeta \sim N(0, \sigma^2)$ , then

$$\begin{aligned}
 E\zeta^{2k-1} &\equiv 0, \quad k = 1, 2, 3, \dots; \\
 E\zeta^{2k} &\equiv 1 \cdot 3 \cdot \dots \cdot (2k-1) \sigma^{2k} = (2k-1)!! \sigma^{2k}, \quad k = 1, 2, 3, \dots
 \end{aligned} \tag{2.9}$$



It can be noted, that in this case no interference fringes will be formed at all—the intensity of illumination will gradually decrease at increasing variance  $\sigma^2$ .

This example shows an ill-posed inverse problem. The problem of interpretation of motion from the structure of the field of interference fringes has solution only if the vibration of the analysed system is harmonic. When the oscillations are non-linear (what is likely in MEMS cantilever dynamics) the interpretation of pattern of fringes is rather complicated.

### 2.1.2 *FEM Analysis of MEMS Cantilever Performing Chaotic Oscillations*

Virtual numerical environment is used for MEMS cantilever by FEM techniques with simulation of optical formation of optical holographic interferogram [5]. The first eight eigenmodes are presented in Fig. 2.8.

Complex dynamic response of the tip of the cantilever is got in case simulation of the dynamics of cantilever under oscillating charge excitation. The displacement of the tip of the cantilever is presented in Fig. 2.9. Various time exposures are used to generate holographic interferograms of the cantilever and the results are presented in Fig. 2.10.

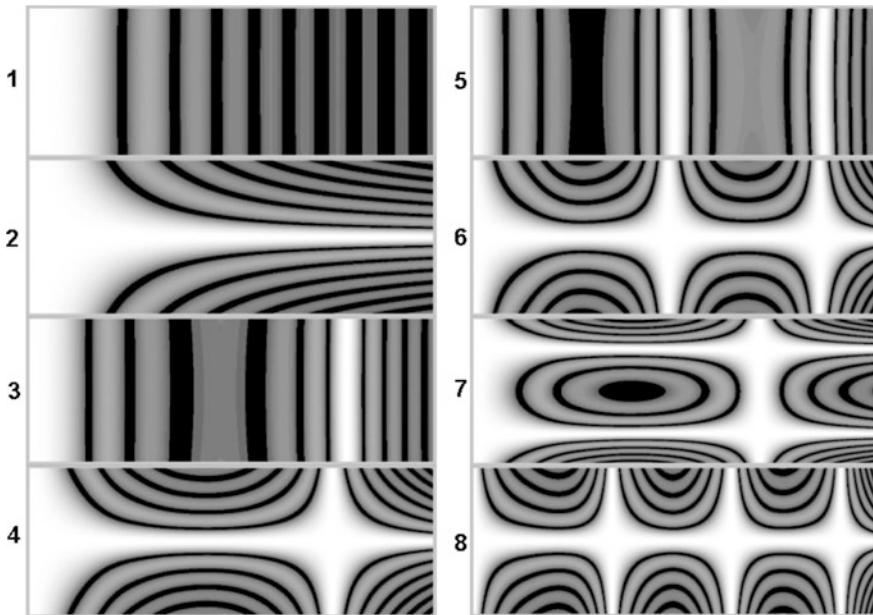


**Fig. 2.8** Time average holographic interferograms of the first eight eigenmodes of MEMS cantilever

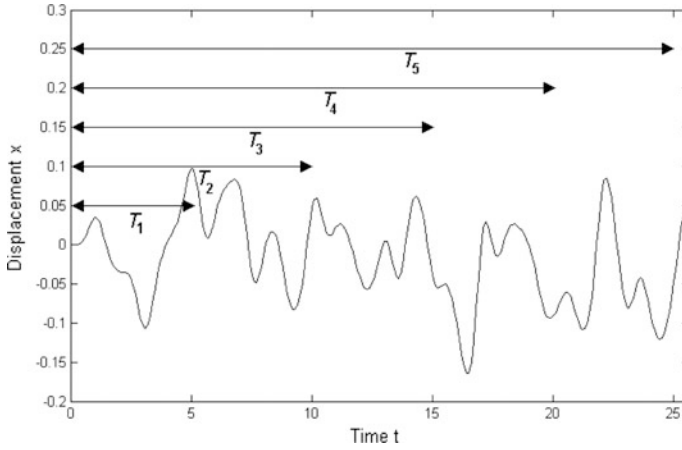
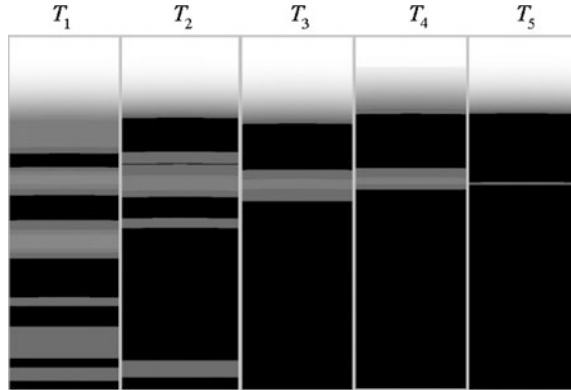


**Fig. 2.9** Chaotic dynamics of the tip of MEMS cantilever and times of exposure  $T_1$ – $T_5$

**Fig. 2.10** Time average interferograms of the MEMS cantilever at different times of exposure



The complexity of the dynamical processes taking place in the analysed MEMS systems is illustrated by presented numerical results which validate the theoretical predictions and help to explain character of MEMS motion.

### 2.1.3 The Structure of Digital Data Processing

Holographic interferometry data processing system is presented in Fig. 2.11.

Box 1 represents the initial data of the analysis—that is, holographic interferogram holding information about the measured object and interference bands which denote the time variance of the surface of the analysed body [6]—Fig. 2.12.

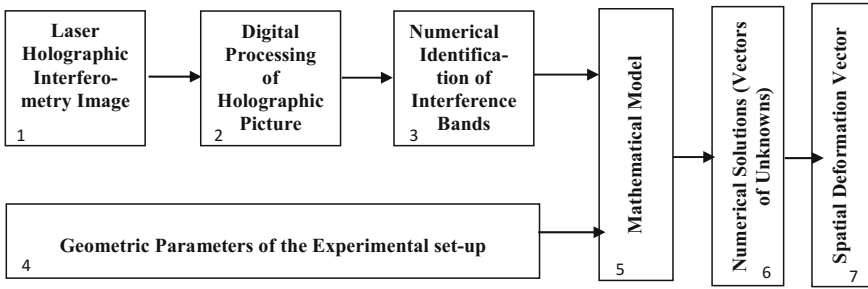


**Fig. 2.11** Structure of data processing system

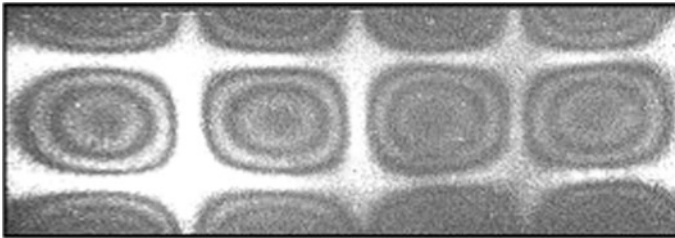


**Fig. 2.12** Laser holographic interferometry image of a vibrating plate

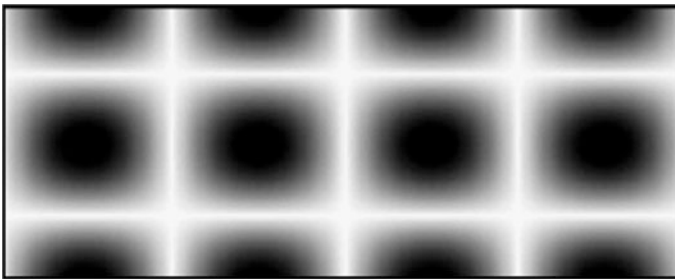


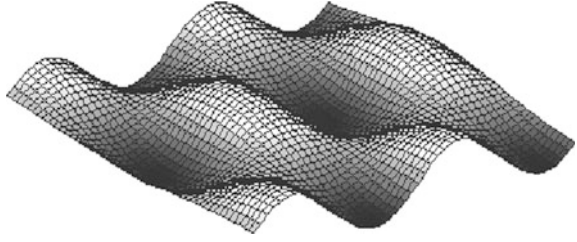
**Fig. 2.13** Digital image of interferogram

Box 2 represents the digital pre-processing of the hologram. The hologram data is scanned into computer by means of digital camera in automated systems, or by means of scanner in smaller scale experimental set-up. The digital image is filtered using noise rejection and intensity balancing algorithms [6].

Numerical identification of interference bands in the pre-processed digital image is presented in Box 3 (Fig. 2.13). The output of this step is used as a direct input for the mathematical model processing algorithm (Box 5).

As the formation of interference bands is highly dependent on the geometrical parameters of the experimental set-up, these parameters are a priori calculated

**Fig. 2.14** Deformation vector of the vibrating plate



before the experiment and feeded into mathematical model algorithm (Box 5) together with the data of interference bands [7, 8]. That's why the developed interferometry data identification system is especially suitable for automated control system—once the geometrical parameters are defined for a certain type of object, the further analysis of a series of objects may be fully automatised as seen from Fig. 2.11.

When the mathematical model is formed, numerical finding vector of unknowns is performed (Box 6) [9]. Further the quantitative parameters of the object's change may be presented in the graphical format (Box 7)—Fig. 2.14.

### 2.1.4 The Mathematical Model of the Optical Measurement

The geometry of used vibration measurement scheme is presented in Fig. 2.15, where  $i$  some point with the axes  $r, t, z$  of the orthogonal system shown.

$R$  is the vector of spatial vibrations of the  $i$ -th point of the pjezo transformer;  $U, V, W$  are the components of the vector of spatial vibrations of the  $i$ -th point in the directions of the coordinate axis  $r, t, z$ , respectively;  $l$  is the unit vector of lightening of point  $i$ ;  $m$  is the unit vector of observation of point  $i$ ;  $\alpha, \beta$  are the angles of unit vectors of lightening and observation with the coordinate axis  $r$ , respectively;  $\gamma, \theta$  are the angles between the coordinate axis  $z$  and the unit vectors of lightening and observation, respectively.

We consider that the spatial vibrations of the surface point  $i$  of the analysed body are described as:

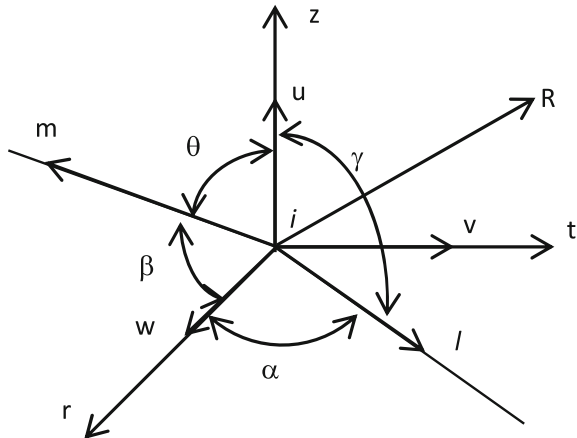
$$\bar{R}_i(\tau) = U_i(\tau)\hat{i} + V_i(\tau)\hat{j} + W_i(\tau)\hat{k} \quad (2.10)$$

where  $\tau$  is time.

The tangential  $U, V$  and normal  $W$  components of the vector  $\bar{R}_i(\tau)$  at the point  $i$  are expressed as follows

$$\begin{aligned} U(\tau) &= U_0^i \cos(\omega\tau + \alpha_i), & V(\tau) &= V_0^i \cos(\omega\tau + \beta_i), \\ W(\tau) &= W_0^i \cos(\omega\tau + \gamma_i) \end{aligned} \quad (2.11)$$

**Fig. 2.15** The scheme of optical measurement



where  $U_0^i, V_0^i, W_0^i$  are the amplitudes of forced vibrations at point  $i$  in coordinates  $r, t, z$ , respectively.

The amplitudes of forced vibrations are expressed by representing them through the eigenmodes of vibrations [10]:

$$\begin{aligned} U_0^i &= \sum_{j=1}^k A_j^u F_{ij}^u; \\ V_0^i &= \sum_{j=1}^k A_j^v F_{ij}^v; \\ W_0^i &= \sum_{j=1}^k A_j^w F_{ij}^w; \end{aligned} \quad (2.12)$$

where  $F_{ij}$  is the amplitude value of the  $j$ -th eigenmode of vibration at point  $i$ , which is calculated according to the analytical expressions by taking into account the conditions of fastening of the analyzed body,  $A_j$  is the influence coefficient of the  $j$ -th eigenmode of vibrations,  $k$ —the number of given eigenmodes of vibrations; of course, by taking into account the presented relationships it is clear that in order to calculate the components of the vector of spatial vibrations it is necessary to determine  $F_{ij}^u, F_{ij}^v, F_{ij}^w, A_j^u, A_j^v, A_j^w, \alpha_i, \beta_i, \gamma_i$ .

The values  $F_{ij}^u, F_{ij}^v, F_{ij}^w$  are calculated according to the known analytical expressions that are used in theory of vibrations for the calculation of the amplitudes of vibrations of eigenmodes by taking into account the geometry of the body analyzed and the boundary conditions of its fastening [9].

The parameters  $A_j^u, A_j^v, A_j^w, \alpha_i, \beta_i, \gamma_i$  are to be determined from the measured experimental data.

According to the characteristic function of distribution of the interference bands on the surface the following nonlinear algebraic equation is constructed:

$$\frac{\Omega^i \lambda^2}{4\pi} = \left[ \begin{aligned} & \left( \sum_{j=1}^k A_j^w F_{ij}^w \right) \cos \gamma_i K_r^i \\ & + \left( \sum_{j=1}^k A_j^v F_{ij}^v \right) \cos \beta_i K_t^i \\ & + \left( \sum_{j=1}^k A_j^u F_{ij}^u \right) \cos \alpha_i K_z^i \end{aligned} \right]^2 + \left[ \begin{aligned} & \left( \sum_{j=1}^k A_j^w F_{ij}^w \right) \sin \gamma_i K_r^i \\ & + \left( \sum_{j=1}^k A_j^v F_{ij}^v \right) \sin \beta_i K_t^i \\ & + \left( \sum_{j=1}^k A_j^u F_{ij}^u \right) \sin \alpha_i K_z^i \end{aligned} \right]^2 \quad (2.13)$$

where  $\lambda$  is wavelength of the laser lighting;  $\Omega$  is calculated from the holographic interferograms at the centers of dark interferential bands;  $K_r^i, K_t^i, K_z^i$  are the projections of the sensitivity vector that are calculated by taking into account the optical scheme of the holographic measurement.

The nonlinear algebraic Eq. (2.13) is solved according to the method presented in [10]. Thus, the following equation is derived from time average holographic interferogram data:

$$f_i = \left[ \begin{aligned} & \left( \sum_{j=1}^k A_j^w F_{ij}^w \right) \cos \gamma_i K_r^i \\ & + \left( \sum_{j=1}^k A_j^v F_{ij}^v \right) \cos \beta_i K_t^i \\ & + \left( \sum_{j=1}^k A_j^u F_{ij}^u \right) \cos \alpha_i K_z^i \end{aligned} \right]^2 - \left[ \begin{aligned} & \left( \sum_{j=1}^k A_j^w F_{ij}^w \right) \sin \gamma_i K_r^i \\ & + \left( \sum_{j=1}^k A_j^v F_{ij}^v \right) \sin \beta_i K_t^i \\ & + \left( \sum_{j=1}^k A_j^u F_{ij}^u \right) \sin \alpha_i K_z^i \end{aligned} \right]^2 - \left[ \frac{\Omega_i}{n} \right]^2 \quad (2.14)$$

We differentiate the obtained equation with respect to the unknowns and construct a matrix the columns of which will be respectively

$$G_j^{(i)} = \frac{\partial f_i}{\partial A_j^u}; \quad G_{j+k}^{(i)} = \frac{\partial f_i}{\partial A_j^v}; \quad G_{j+2k}^{(i)} = \frac{\partial f_i}{\partial A_j^w}; \quad j = 1, 2, \dots, k; \quad (2.15)$$

$$G_{1+3k}^{(i)} = \frac{\partial f_i}{\partial \alpha_i}; \quad G_{2+3k}^{(i)} = \frac{\partial f_i}{\partial \beta_i}; \quad G_{3+3k}^{(i)} = \frac{\partial f_i}{\partial \gamma_i};$$

If the number of holographic interferograms is made for the point  $i$  for different angles of lightening is  $q$  and the total number of the data sets is formed, then the dimensions of the matrix  $G$  will be  $q \times 3(2k + 3)$  [10].

For the given vector of unknowns

$$B = (A_1^u, A_2^u, \dots, A_k^u, A_1^v, A_2^v, \dots, A_k^v, A_1^w, A_2^w, \dots, A_k^w, \alpha, \beta, \gamma) \quad (2.16)$$

we will seek for the solution of nonlinear algebraic equation by using iterations in the following form:

$$\sigma = \Gamma^{-1}P$$

$$\Gamma_{1j} = \sum_{i=1}^q G_1^{(i)} G_j^{(i)}; \quad P_j = - \sum_{i=1}^q f_i G_j^{(i)}, \quad j = 1, 2, \dots, (3 + 3k) \quad (2.17)$$

Numerical solution of Eq. (2.17) produces a spatial deformation vector, which may be represented in a graphical format. The solution of the system enables the reconstruction of special surface deformations of the measured object.

### 2.1.5 *Vibration-Assisted Spring-Loaded Micro Spray System. Design and Principle of Operation*

The spring-loaded microspray system for drug supplying in vessels is presented. The spring-loaded microspray system consist from the rigid steel spring made of turns without gaps and capable to ensure the system tightness in case of drug supplied under fixed pressure to the sealed spring. The spring-loaded batcher is shown in Fig. 2.16.

Let us suppose that the inlet opening of the spring-loaded microspray system is at the middle of the spring. Another end of the spring *1* is tightened and fixed to transverse vibration vibrator *4*.

When the spring is at rest it does not leak out the liquid drug between the turns (the close contact between the turns provides the tightness of the spring).

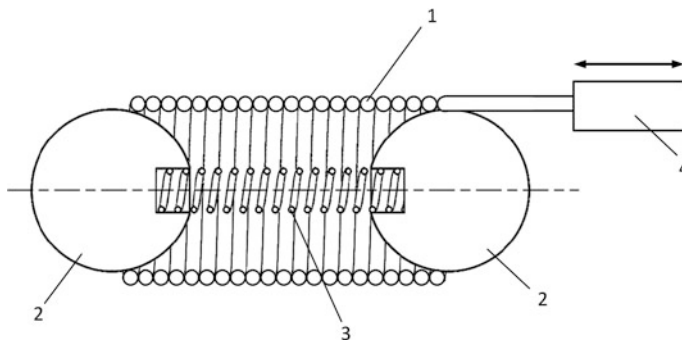


**Fig. 2.16** Spring-loaded microspray system: *1* spring; *2* ball; *3* connecting spring; *4* transverse vibration vibrator

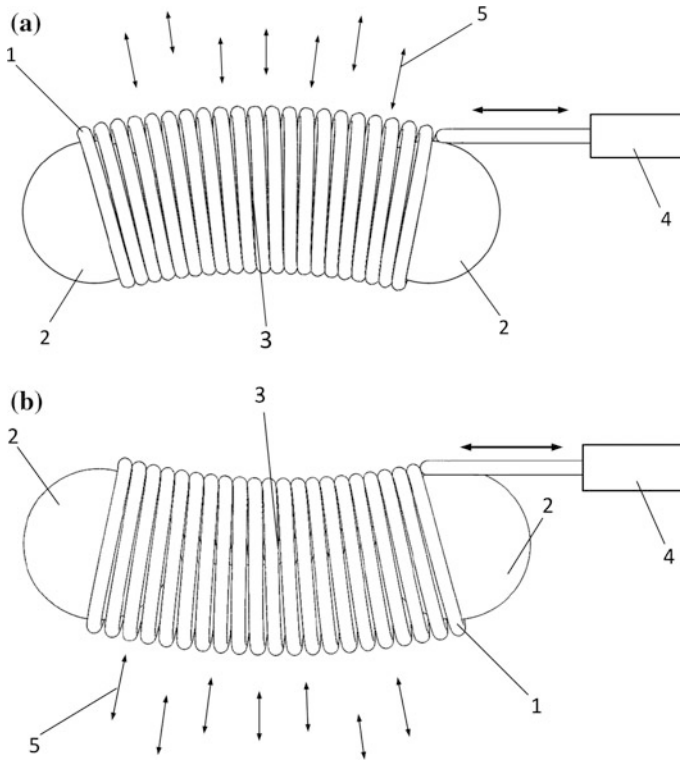


**Fig. 2.17** Spring loaded micro spray system: **a** micro spray to spring moving *upper* direction; **b** micro spray at spring is moved to *down* position

Then, when the transverse vibrations are excited by the help of the vibrator in the form of standing wave in the spring, the spaces between the turns appear, which provide the possibilities for the drug leak out. The half-wave are excited in order to ensure that their amplitude peak phases appeared at the liquid centers of inlet manifold (Fig. 2.17).

It is obvious, that when the piston moves down the rarefaction is caused, which intakes the liquid drug into the vessels.

This is shown only one of the possibilities to arrange the spring loaded micro spray system. The other solution could be to arrange the spring-loaded system in case when we need to excite transverse vibrations, e.g. in the shape of a single half-wave. This would provide the possibility for a separate spring micro spray system loaded to operate independently.



### 2.1.6 Theoretical Substantiation of Possibilities for the Batcher Functioning

The rigid coiled spring could be considered as a duct. Let us suppose, that within the range of spring strains analyzed, the material elasticity is constant, therefore, dependence on the strain amount from the applied force is directly proportional. If the spring is affected by the axis strength force, the existing winding area will be proportional to the spring elongation.

The increased surface of elongated spring will be determined, when it is coiled into the arc. The calculation scheme is presented in Fig. 2.18. In the inner part of bended spring the turns touch each other tightly. Hence the inner arc curvature range is  $\rho_0$ . It is equal to:

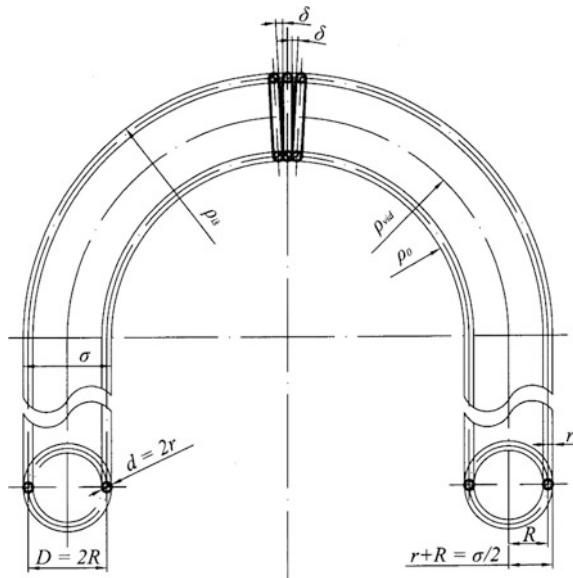
$$\rho_0 = \frac{L}{\pi}. \quad (2.18)$$

The length of the arc  $L$  is equal to:

$$L = \frac{2\pi\rho_0}{2} = \pi\rho_0. \quad (2.19)$$

The outer part of the arc between the turns will have the gap  $\delta$ , which being in the shape of spiral, decreases to 0 in the inner part of the arc. Thus, the gap of spiral shifting width gap is produced.

**Fig. 2.18** Calculation scheme of the spring elongation



The outer arc radius  $\rho_{ext}$  is equal:

$$\rho_{ext} = \rho_0 + 2(R + r). \quad (2.20)$$

The outer arc length  $L_{ext}$  is:

$$L_{ext} = \pi \rho_{ext} = \pi[\rho_0 + 2(R + r)] = \pi(\rho_0 + \sigma), \quad (2.21)$$

where,  $\sigma$ —spring-duct diameter. It is equal to:

$$\sigma = 2(R + r). \quad (2.22)$$

Thus outer arc length  $L_{ext}$  is:

$$L_{ext} = \pi \left( \frac{L}{\pi} + \sigma \right) = L + \pi \sigma. \quad (2.23)$$

Outer arc elongation  $\Delta L$  is equal to:

$$\Delta L = L_{ext} - L = L + \pi \sigma - L = \pi \sigma. \quad (2.24)$$

Thus average elongation of the spring  $\Delta L_{ave}$  is equal to:

$$\Delta L_{ave} = \frac{\Delta L}{2} = \pi(8 + r). \quad (2.25)$$

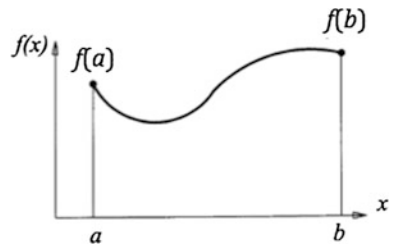
Increased surface of average elongated spring  $\Delta S_{ave}$  will be equal to:

$$\Delta S_{ave} = 2\pi R \Delta L_{ave} = 2\pi^2 R(R + r). \quad (2.26)$$

This is the space for the leak out of the part of fuel.

Let us analyze the case, when the spring-duct axis is in the shape of curve, which is presented in Fig. 2.19.

**Fig. 2.19** Spring axis as curve



In general case between  $f(a)$  and  $f(b)$ :

$$l = \int_a^b \sqrt{1 + [f'(x)]^2}. \quad (2.27)$$

If the excited vibrations are in the shape of sine, the half of its length  $L_p$  will be (Fig. 2.19):

$$L_p = \int_0^{1/4} \sqrt{1 + [\sin' x]^2} = \int_0^{1/4} \sqrt{1 + \cos^2 x}. \quad (2.28)$$

The spring-duct elongation half-waves  $\Delta L_p$  will be:

$$\Delta L_p = L_p - \frac{l}{4}. \quad (2.29)$$

This elongation of the spring affects the increase of its inner surface:

$$\Delta S_{ave} = 2\pi R \Delta L. \quad (2.30)$$

Thus, the outer surface  $S$  area change could be expressed as:

$$S = A_0 \cos\left(\frac{2\pi}{\lambda}x\right) \sin(2\omega t), \quad (2.31)$$

$$\omega = 2\pi f, \quad (2.32)$$

where:  $A_0$ —maximum amplitude of standing waves;  $x$ —spring-duct coordinate along axis;  $\lambda$ —length of wave;  $f$ —frequency, Hz.

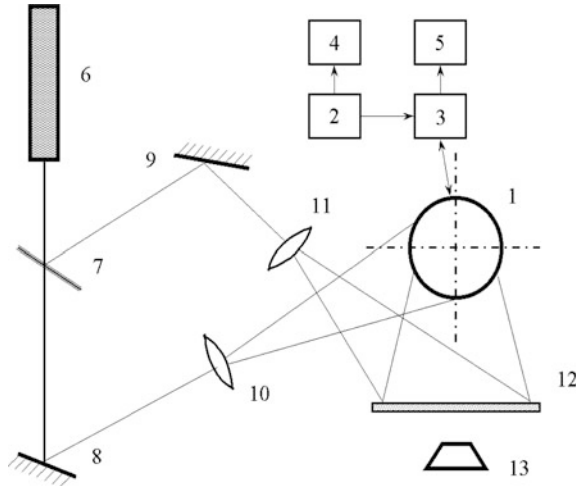
Thus, we could confirm, that the higher the amplitude of spring vibration, the wider the space between the spring turns and more fuel will leak out between them.

### 2.1.7 Experimental Analysis of the Spring

In order to calculate amplitude of vibrating spring the methodology is presented in papers [7, 9, 10].

In Fig. 2.20 it is shown optical scheme for recording holographic interferograms of the vibrating spring: 1—vibrating spring; 2—high-frequency signal generator; 3—amplifier. The signal monitoring means are; 4—frequency meter, 5—the voltage amplitude of the power supply is monitored by the voltmeter. The optical scheme includes a holographic table with a helium-neon laser which serves as a

**Fig. 2.20** Optical scheme of the laser holographic interferometry system: 1 tubular working tube, 2 high-frequency signal generator, 3 amplifier, 4 frequency meter, 5 voltmeter, 6 laser, 7 beam splitter, 8, 9 mirror, 10, 11 lens, 12 photographic plate, 13 recorder



source of coherent radiation. At first the beam from the optical laser 6 splits into two coherent beams and one of them is passing through the beam splitter 7. The another one, so called object beam, reflected from the mirror 8, and widespread lens 10 and illuminates the surface of the vibrating spring 1 and, after reflecting from it, illuminates the photographic plate 12. The reference beam, reflected by the mirror 9, and by the lens 11, illuminates the holographic plate 12 where the interference of these two beams is recorded.

The characteristic function defining distribution interference on the surface of the vibrating spring is presented in (2.33).

$$M_T = \lim_{T \rightarrow \infty} \frac{1}{T} \int_0^T \exp \left( i \left( \frac{4\pi}{\lambda} \right) Z(x) \sin \omega t \right) dt = J_0 \left( \left( \frac{4\pi}{\lambda} \right) Z(x) \right) \quad (2.33)$$

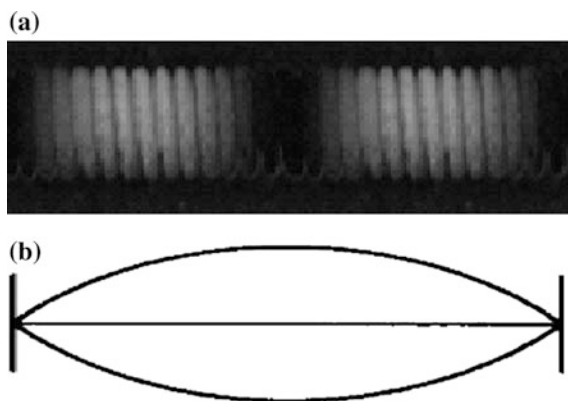
where  $T$ —the exposure time vibrating spring onto the hologram, ( $T \gg 1/\omega$ );  $\omega$ —the frequency of vibration of spring,  $\lambda$ —the laser wavelength of used for recording holographic interferogram;  $J_0$ —zero order Bessel function of the first type.

Then, the resulting intensity  $I$  of the point  $(x, y)$  on the holographic interferogram of vibrating spring is follows:

$$I(x, y) = a^2(x, y) |M_T|^2, \quad (2.34)$$

where  $a(x, y)$  defines the distribution of the amplitude of the incident laser beam. The usage of the method of time averaging holographic interferometry allows to measure steady state vibration. Results of experimental analysis vibrating spring are presented in Fig. 2.21.

**Fig. 2.21** Results of experimental analysis: holographic interferogram of vibrating spring at frequency 1.24 kHz **a**, distribution amplitude of vibration of spring **b**



## 2.2 Numerical–Experimental Method for Evaluation of Geometrical Parameters of Periodical Microstructure

Optical modulator is a device that modulates or varies the amplitude of an optical signal in a controlled manner. Optical modulator generates desired intensity, color and the like in the passing light by changing optical parameters such as the transmission factor, refractive index, reflection factor, degree of deflection and coherency of light in the optical system according to the modulating signal. A constituent part of the modulator is a diffractive optical element (DOE).

Different methods and materials are used to produce diffraction gratings for DOEs. On the other hand two-dimensional or three-dimensional periodic structures of micrometer-scale period are widely used in microsystems or their components, e.g. as elements of micro-fluidic devices. Long deep groves (in optical terms—phase diffraction grating) can be used as elements for microscale synthesis, processing, and analysis of chemical and biological samples that require manipulation of microscopic volumes of liquids. Usually this can be accomplished with chips with micro-channels and microreactors.

Replication technologies such as embossing, molding and casting are highly attractive for the fabrication of surface relief holograms and diffractive optical elements microstructures [11]. The combination of replication technology with other processes such as dry etching and thin film coating can offer new possibilities in the mass production. The major replication technologies that are in use today [hot embossing, injection molding and casting (or UV embossing)] employ different types of polymers. Polymers are receiving global attention for a myriad of planar photonic and optoelectronic applications including optical interconnects [12], switches [13], splitters [14], and surface relief structures [15]. This is a direct result of the relative ease and cost effectiveness with which planar polymeric structures can be fabricated, with respect to semiconductor and oxide analogs, while maintaining the requisite performance levels.

For characterization of geometrical parameters of such microrelief structures usually various construction microscopes are used, mostly scanning electron or probe microscopes [16]. These direct methods are sometimes destructive and hardly can be employed for in situ analysis. Therefore indirect optical interference or diffraction methods are used widely [17].

Measuring diffraction efficiency for the visible light is known as an indirect method to evaluate geometrical parameters of diffraction gratings [18, 19]. Diffraction efficiency is one of the crucial properties of the optically variable devices such as kinegrams or 3D holograms [20] that are used widely during last decade to provide document security [20]. High efficiency diffraction grating is important as well in a variety of applications, such as optical telecommunications, lithography, and laboratory spectroscopy [21].

From this point of view optical methods are very flexible and efficient in control where dimensions of periodic structures are in micrometer range.

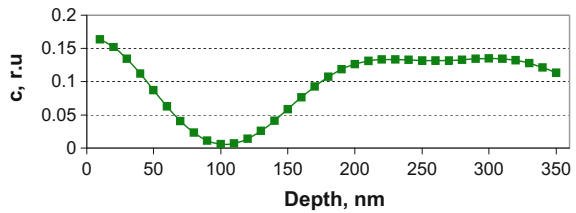
### 2.2.1 Concept of Indirect Method for Evaluation of Geometrical Parameters of Periodical Microstructure

All periodical microstructures formed in optical materials are characterized by relative diffraction efficiencies. Relative diffraction efficiency  $RE_{i,j}$  is defined as ratio of intensity of diffracted light  $I_{i,j}$  to the  $i$ -th diffraction maxima and  $j$ -th illumination angle with intensity  $I_j$  of reflected light or transmitted through specimen without micro relief to  $j$ -th illumination angle:

$$RE = \frac{I_{i,j}}{I_j}. \quad (2.35)$$

Comparison of modeled diffraction efficiencies with experimental results could be used to control variation of geometrical parameters of periodical microstructure during technological process. Difference  $c_{SE}$  (Fig. 2.22) between numerical and experimental results is calculated using least squares method:

**Fig. 2.22** Difference  $c$  versus depth of periodical microstructure (sinusoidal profile period  $d = 4 \mu\text{m}$ ) for green laser ( $\lambda = 532 \text{ nm}$ )



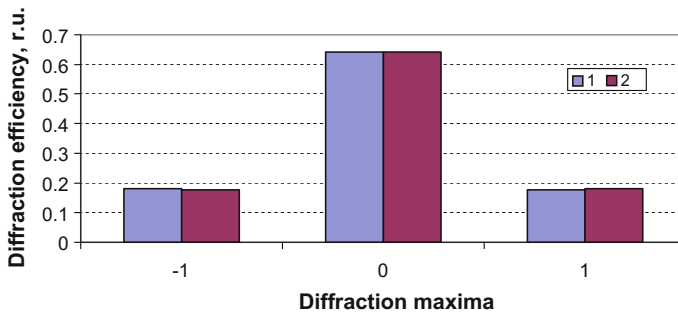


**Fig. 2.23** Experimental (1) and theoretical (2) relative diffraction efficiencies of periodical microstructure (sinusoidal profile, depth 105 nm, period  $d = 4 \mu\text{m}$ ) for the green laser ( $\lambda = 532 \text{ nm}$ )

$$c = \frac{1}{k \cdot n} \sum_{j=1}^k \sum_{i=1}^n \left( RE_{i,j}^T - RE_{i,j}^E \right)^2; \quad (2.36)$$

$RE_{i,j}^T, RE_{i,j}^E$ —numerical and experimental relative diffraction efficiencies to the  $i$ -th diffraction maxima and  $j$ -th illumination angle.

Depth of periodical microstructure is in the minimum point of curve  $c$ , where the difference between experimental and numerical results is the smallest. Application of this method enables evaluation of geometrical parameters with an error of less than 5%. Good fit of experimental and theoretical relative diffraction efficiencies of periodical microstructure (sinusoidal profile, depth 105 nm, period  $d = 4 \mu\text{m}$ ) for green laser ( $\lambda = 532 \text{ nm}$ ) is illustrated in Fig. 2.23. Calculations were confirmed with atomic force microscope NANOTOP 206.

This method could be used for the non-destructive control of variation of geometrical parameters of periodical microstructure during technological process.

### 2.2.2 Evaluation of Geometrical and Optical Parameters of Periodical Microstructure

Figure 2.24 presents AFM photographs of a matrix in silicon (a), matrix polymer replica (b), matrix in nickel stamp (c) and matrix hot embossed in Al metalized PMMA layer on PET (d). Table 2.1 summarises the main parameters [period ( $d$ ), depth ( $h$ ) and modulation coefficient ( $\mu$ )] of the investigated diffraction gratings. The columns denoted as “Measured by AFM” present experimental values of the grating. As one can see modulation of the diffraction grating is lost during the replication steps.

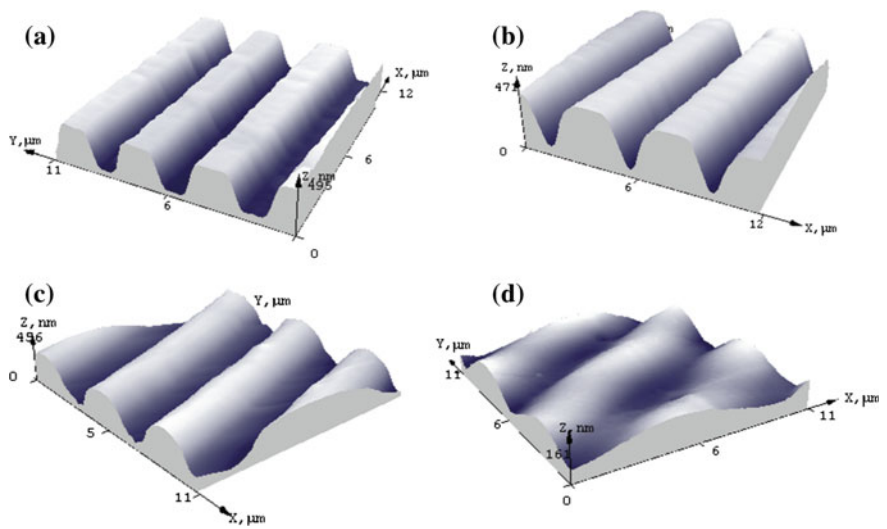


**Fig. 2.24** *Top-left* AFM photographs of matrix in silicon. *Top-right* matrix polymer replica. *Bottom-left* matrix in nickel stamp. *Bottom-right* matrix hot embossed in Al metalized PMMA layer on PET

**Table 2.1** Main parameters of the investigated diffraction gratings

Diffraction grating	Period d, μm		Depth h, μm		Modulation, $\frac{h}{d}$	Groove profile
	Measured by AFM	Simulated	Measured by AFM	Simulated		Measured by AFM
Si master-matrix	4	4.1	0.5	0.535	0.125	Trapezoidal
UV replica	4.2	4.1	0.47	–	0.112	Trapezoidal
Ni stamp	4.2	4.1	0.4	–	0.095	Sinusoidal
Replica T = 120 °C	4.4	4.3	0.2	0.195	0.045	Sinusoidal

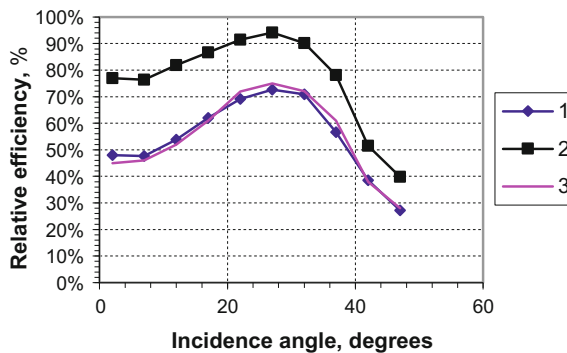
UV curing plays an important role in cementing of optics or for fabrication of replicated optics [21]. For replicated optics, shrinkage and form modifications are usually measured by comparing the replica to the mould geometry after the curing process has finished [17]. One can see that, producing of UV replica is related to the production of the reverse grating of the silicon matrix with the higher value of the period. This fact is known [22, 23] and is related to the expansion of UV replica. According to [23] in the case of big patterns, a large amount of resist has to be displaced over a large distance. Thus the polymer in the middle of these patterns does not flow but it is compressed and stores stresses. This compressed polymer reacts elastically and when the force is removed, it recovers.



The biggest losses of the modulation are found during the thermal embossing process. It should be noted as well that originally trapezoidal diffraction grating during production of the Ni stamp and hot embossing is transformed to the sinusoidal one.

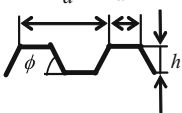
To follow variations of the geometrical parameters, the diffraction efficiencies of the periodic structures were registered after the main technological steps. Figure 2.25 (curves 1, 2) illustrates experimental dependence of the relative efficiency of the first diffraction maximum ( $RE_1$ ) and all maxima ( $RE_S$ ) versus angle of incidence for the silicon master matrix. Angles of incidence were varied between  $2^\circ$  and  $47^\circ$ . Curve 3 (Fig. 2.25) illustrates variation of the relative efficiency as simulated with the PCGrate-SX6.0 programme. During these calculations trapezoidal diffraction grating in silicon was considered as rectangular one and the ridge width as well as depth of the grating was varied systematically to fit the experimental curve (2) in Fig. 2.25. Geometrical parameters of the simulated grating are presented in Table 2.2 where they are compared with the corresponding parameters of the silicon master matrix measured by AFM. Such an approach allows to calculate angular dependence of the relative diffraction efficiency with high determination coefficient ( $R^2 = 0.99$ ) and to reconstruct the geometrical parameters of the diffraction grating from the optical measurements with accuracy better than 10%. In such evaluations diffraction efficiency of the first diffraction maximum is informative enough and higher maxima may be ignored during the consideration.

Changes in the shape of periodic structure during the replication can be easily detected by measuring angular dependence of the diffraction efficiency as it is shown in Fig. 2.26. In this case angular dependences of diffraction efficiencies of the structure (presented in Fig. 2.24) are depicted (curve (1) corresponds to the Si master matrix, curve (2)—matrix in the stamp, curve (3)—matrix embossed in



**Fig. 2.25** Relative efficiencies of the diffraction grating in silicon (master matrix) ( $d = 4 \mu\text{m}$ ,  $h = 0.5 \mu\text{m}$ ,  $a = 1.9 \mu\text{m}$ ) versus angle of incidence: (1) experimentally measured for the first diffraction maximum, (2) experimentally measured for the six diffraction maxima, and (3) computer simulated for the first diffraction maximum

**Table 2.2** Comparison of the simulated geometrical parameters of the silicon master matrix with the corresponding parameters measured by AFM

Material	Results	Period d, $\mu\text{m}$	Ridge width, a		Side wall deviation angle, $\phi$	Depth h, $\mu\text{m}$	
			$\mu\text{m}$	r.u. <sup>a</sup>			
Crystalline Si(100)	Measured by AFM	4	1.9	0.48	82°	0.5	
	Simulation	4.1	2.1	0.51	90°	0.535	

<sup>a</sup>Ridge width in r.u. is calculated as  $\frac{a}{d}$

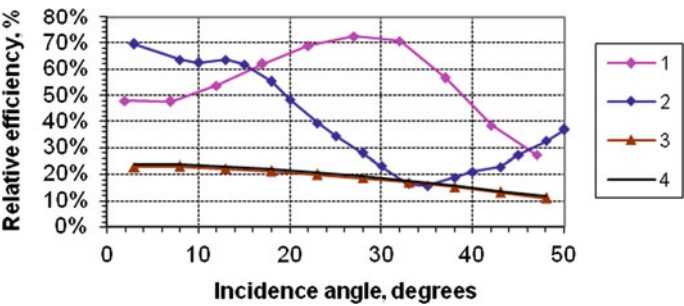


**Fig. 2.26** Angular dependencies of the relative efficiencies of the diffraction grating measured at different technological steps: 1—Si master matrix, 2—nickel matrix, 3—matrix hot embossed in Al metalized PMMA layer on PET, 4—simulated diffraction grating

Al/PMMA structure). Curve (4) presents calculated angular dependence of the grating produced in Al/PMMA structure using the experimentally defined (by AFM) parameters of the grating. One can see that low modulation values (as it is defined from the AFM measurements, Table 2.1) bring to the low value of diffraction efficiency. High value of determination coefficient (0.95) for the experimental curve (3) and simulated curve (4) illustrate that sinusoidal profile describes well the real profile of the grating. A column “Simulated” in Table 2.1 summarizes main results of the computer simulation that can be compared with the AFM measurement results.

Such an approach appears as an efficient method to analyze hot embossing process. Figure 2.27 presents the dependence of the relative diffraction efficiency versus embossing temperature at constant angle of incidence of analyzing light. Figure 2.28 illustrates angular dependencies of the relative efficiency for two temperatures of embossing. In all investigated cases [different periods of diffraction grating curves (1, 2) and curves (3, 4) and different temperatures of embossing curves (1, 3) and (2, 4)] relative efficiency of resultant replica in Al/PMMA are well described by sinusoidal profile (as it was shown in Fig. 2.26). One can see (Fig. 2.27) that sinusoidal profile from Ni matrix is transferred efficiently to the

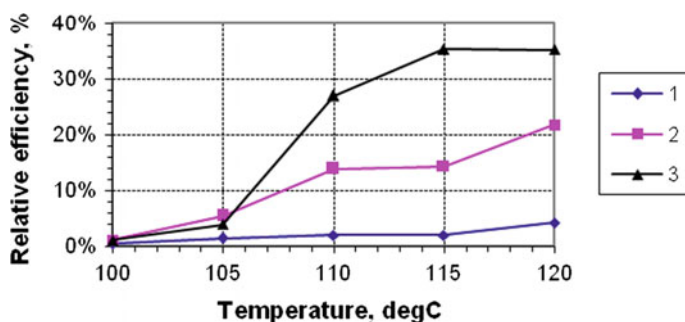


**Fig. 2.27** Dependence of the relative diffraction efficiency versus embossing temperature for the gratings of  $h = 0.5 \mu\text{m}$  and different period: 1— $d = 2 \mu\text{m}$ , 2— $d = 4 \mu\text{m}$ , 3— $d = 5.6 \mu\text{m}$  (angle of incidence of light  $3^\circ$ )

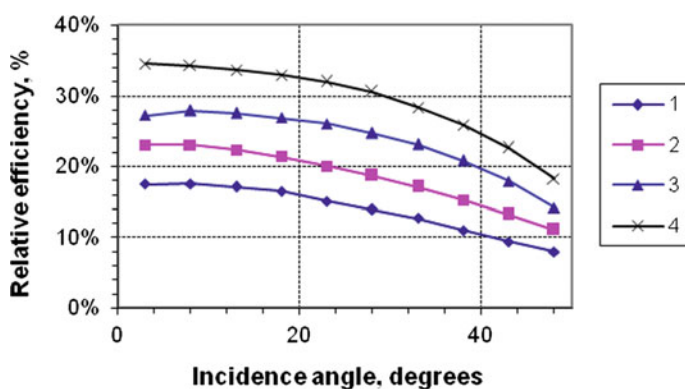


**Fig. 2.28** Angular dependencies of relative efficiencies of gratings of  $h = 0.5 \mu\text{m}$  and different period: 1, 2— $d = 4 \mu\text{m}$ , 3, 4— $d = 5.6 \mu\text{m}$  for two embossing temperatures 1, 3— $T = 110^\circ\text{C}$ , 2, 4— $T = 120^\circ\text{C}$

PMMA within the interval of embossing temperatures 110–120 °C. Within this interval of temperatures relative efficiency reaches maximum value within the technologically compatible processes ( $p = 0.3 \text{ MPa}$ ,  $t = 2 \text{ s}$ ). One can see as well that this process is sensitive to the modulation ratio of the grating. Our measurements reveal well documented fact [24] that in lower temperature range elastic response of the polymer dominates and in the region close to the polymer glass transition temperature plastic flow of the polymer contributes to the efficient shape transfer. According to our optical measurement results keeping constant pressure and time of embossing, rheological properties of polymer are expressed better for the higher period grating. The best relative efficiency was found for the diffraction grating of  $5.6 \mu\text{m}$  period embossed at  $120^\circ\text{C}$  temperature.

### 2.2.3 Evaluation of Geometrical Parameters with High Aspect Ratio

However, when the depth ( $h$ ) of periodic microstructure is higher than the order of coherent radiation wavelength ( $\lambda$ ) used for investigation of depth, the periodical repeatability of theoretical results is obtained (2.29). Therefore there are several sets of geometric parameters with the good agreement to experimental. In this case, without the usage of additional measuring instruments such as atomic force microscopy or scanning electron microscope, it is not possible clearly to identify the depth of the periodic microstructure. Therefore the methodology, based on comparison of optical and numerical results, for determination of deep (micrometers queue depth) periodic microstructures depth was developed

Analyzing the  $RE_{ij}$  dependence on the depth (Fig. 2.29), in the region of the small depth one can see clearly influence of both factors (angle of incidence and wavelength). One can see that applying higher wavelength results in the shift of these dependencies to the right and this shift is more pronounced for the higher angle of incidence.

According to the simulation results (Fig. 2.29), dependence of the relative diffraction efficiency of the zero diffraction maximum versus depth of grating is a periodical function. This phenomenon can be easily understood in terms of optical path length difference produced in the reflection diffraction grating (Fig. 2.30). One can understand that additional optical path length difference distance  $\Delta$  in the phase diffraction grating can be calculated using a geometrical model. This optical path

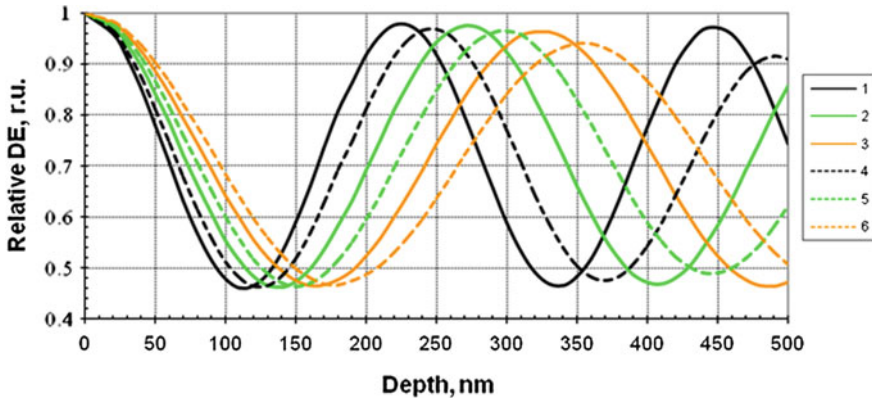
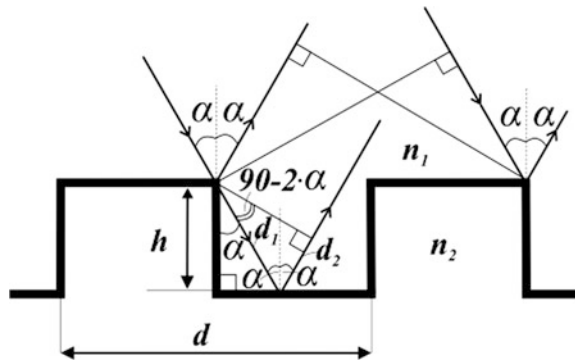


**Fig. 2.29** Simulated dependence of the relative diffraction efficiency of the zero order diffraction maxima on the depth of groove of the phase diffraction grating (diffraction grating in silicon,  $d = 12 \mu\text{m}$ ) for different light wavelength (441.6, 532, 632.8 nm) and incidence angles ( $5^\circ$ ,  $25^\circ$ ): 1—wavelength 441.6 nm and illumination angle  $5^\circ$ ; 2—wavelength 532 nm and illumination angle  $5^\circ$ ; 3—wavelength 632.8 nm and illumination angle  $5^\circ$ ; 4—wavelength 441.6 nm and illumination angle  $25^\circ$ ; 5—wavelength 532 nm and illumination angle  $25^\circ$ ; 6—wavelength 632.8 nm and illumination angle  $25^\circ$

**Fig. 2.30** Geometrical model explaining optical path length difference in a rectangular phase reflection diffraction grating



length difference depends on the incidence angle  $\alpha$ , refractive index of medium ( $n_1$ ) and depth ( $h$ ) of the phase diffraction grating:

$$\Delta = n_1(d_1 + d_2); \quad (2.37)$$

$$\Delta = \frac{n_1 h}{\cos \alpha} (1 + \sin(90 - 2\alpha)). \quad (2.38)$$

One can understand as well that constructive interference condition:

$$\Delta = m\lambda; \quad m = 0, 1, 2, \dots \quad (2.39)$$

will define depth of the diffraction grating (for fixed angle of incidence) where maximum value for the zero maximum will take place. Changing the angle of incidence ( $\alpha$ ) or wavelength will result in the change of  $\Delta$ , and, as a result, change of position of maximum versus depth of the grooves. These dependencies (integer number of wavelengths versus depth of the grating) are summarized in Fig. 2.31.

The cross of the horizontal line (Fig. 2.31) corresponding  $\Delta = 1\lambda$  or  $\Delta = 2\lambda$  in the case of deep grooves allows predicting depth of the grating corresponding to the maximum intensity of the zero maximum (i.e. in this case for 441.6 nm wavelength and  $5^\circ$  illumination angle they correspond to  $h = 0, 220$  and  $440$  nm). These evaluations are in good correlation with the simulation results done with “PCGrate” (Fig. 2.29). One can understand that grating of the different depth then discussed ones will produce maxima at different angle of incidence.

In similar way, depths of diffraction grating providing minimum value of the zero maximum can be easily calculated putting

$$\Delta = (2m + 1)\lambda/2; \quad m = 0, 1, 2, \dots \quad (2.40)$$

This condition defines depth of diffraction grating corresponding to the minimum of the zero order maximum (or maximum of the first order maximum). By the way, this condition defines optimal depth of the diffraction grating working as a beam splitter (zero order maximum is equal to zero and the first order maxima have

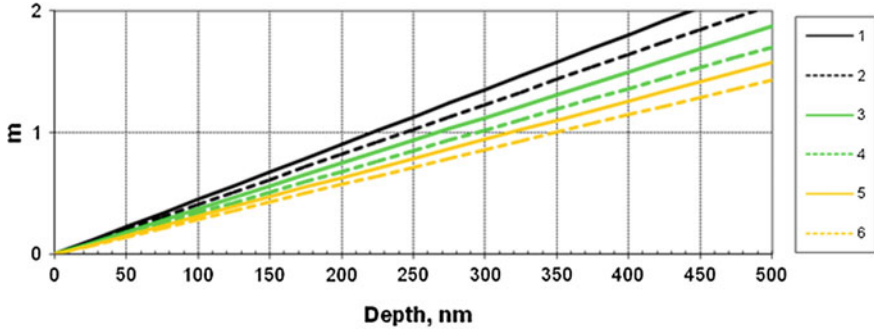


**Fig. 2.31** Number of integer wavelengths in optical path length difference versus depth of the rectangular phase reflection diffraction gratings produced in silicon (calculated for angles of incidence  $5^\circ$ ,  $25^\circ$  and wavelengths 441.6, 532, 632.8 nm): 1—wavelength 441.6 nm and illumination angle  $5^\circ$ ; 2—wavelength 441.6 nm and illumination angle  $25^\circ$ ; 3—wavelength 532 nm and illumination angle  $5^\circ$ ; 4—wavelength 532 nm and illumination angle  $25^\circ$ ; 5—wavelength 632.8 nm and illumination angle  $5^\circ$ ; 6—wavelength 632.8 nm and illumination angle  $25^\circ$

maximal value). This condition in our case looking for the first optimal situation (Fig. 2.29) should be satisfied at the depth equal to 110 nm.

Measuring relative diffraction efficiencies with three wavelengths one can get additional information—relative diffraction efficiency dependence on the wavelength. For example, comparing differences between relative diffraction efficiencies measured with red green and blue light wavelengths we have three additional parameters—differences between relative diffraction efficiencies: for red–green, red–blue, green–blue light. This situation is explained in Fig. 2.32. Combining values of experimental and theoretical relative diffraction efficiencies as well as experimental and theoretical differences between relative diffraction efficiencies measured with different wavelengths one can avoid problems related to the periodical dependence of  $RE_{i,j}$  versus depth. In such case three more parameters related to the different wavelength relative diffraction efficiency should be analyzed:

$$RD_{R-G,j} = \frac{RE_{R,j} - RE_{G,j}}{RE_{R,j}}, \quad (2.41)$$

$$RD_{R-B,j} = \frac{RE_{R,j} - RE_{B,j}}{RE_{R,j}}, \quad (2.42)$$

$$RD_{G-B,j} = \frac{RE_{G,j} - RE_{B,j}}{RE_{G,j}}, \quad (2.43)$$

where:

$RD_{R-G,j}$

is relative difference between relative diffraction efficiencies of zero maxima for wavelengths 632.8 and 532 nm;

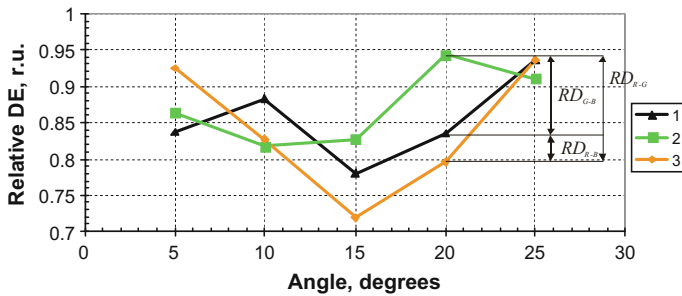


**Fig. 2.32** Dependence of the experimental relative diffraction efficiencies of zero order maxima measured with three lasers (632.8, 532, 441.6 nm) versus illumination angle: 1—wavelength 441.6 nm, 2—wavelength 532 nm; 3—wavelength 632.8 nm

$RD_{R-B,j}$  is relative difference between relative diffraction efficiencies of zero maxima for wavelengths 632.8 and 441.6 nm;  
 $RD_{G-B,j}$  is relative difference between relative diffraction efficiencies of zero maxima for wavelengths 532 and 441.6 nm;  
 $RE_{R,j}$ ,  $RE_{G,j}$  and  $RE_{B,j}$  are relative diffraction efficiencies of zero maxima for red, green and blue lasers.

### 2.2.4 Investigation of Microstructures of High Aspect Ratio

Validation of the proposed model was performed on a system of channels of the micro-fluidic device (reflecting diffraction grating). SEM view of the fabricated micro-fluidic device in silicon is demonstrated in Fig. 2.33. According to the SEM measurements, the period of microchannels was 12  $\mu\text{m}$ , ridge width 9  $\mu\text{m}$  and groove width 3  $\mu\text{m}$ .

The modeling results of reflection diffraction grating were used for indirect depth evaluation of the deep periodic structures—micro-fluidic device in silicon. Two approaches were used for the depth determination of microstructures:

I—comparing values of theoretical and experimental relative diffraction efficiencies  $RE_{i,j}$  for three different wavelengths ( $\lambda \in (632.8, 532, 441.6 \text{ nm})$ ) and five values of incidence angle ( $j \in (5^\circ, 10^\circ, 15^\circ, 20^\circ, 25^\circ)$ ).

II—comparing experimental and theoretical differences between relative diffraction efficiencies ( $RD_{R-G,j}, RD_{R-B,j}, RD_{G-B,j}$ ) obtained with three different wavelengths for five values of incidence angle ( $j \in (5^\circ, 10^\circ, 15^\circ, 20^\circ, 25^\circ)$ ).

In the first case experimental values of angular dependence of relative diffraction efficiency of the second, first and zero order maxima were compared with the computer simulated ones for different depth of diffraction gratings for various illumination angles of visible light.

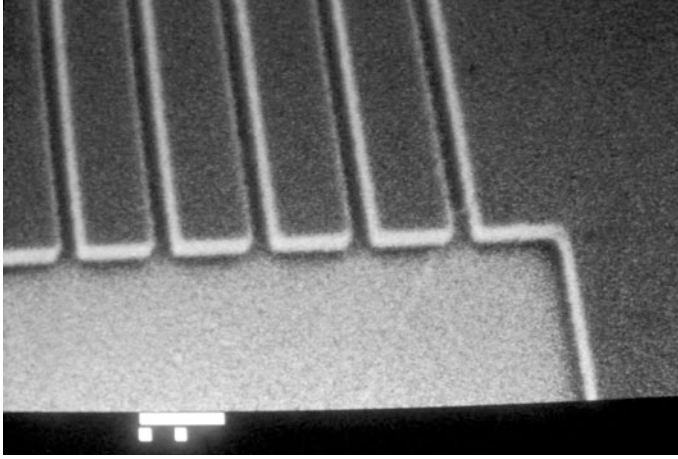


**Fig. 2.33** SEM view of channels of micro-fluidic device (the reservoir connecting the channel system), scale bar 10  $\mu\text{m}$

During this process we have calculated the coefficients of correspondence to the different depth  $c_{depth,j}^{RE}$  of simulated diffraction gratings (for different irradiation angles) to the corresponding experimental values of relative diffraction efficiency (2.44). To find the depth of the grooves these coefficients calculated for different irradiation angles were averaged and average value  $(a_{depth}^{RE})$  was calculated according to (2.45). The dependence of average of coefficients versus range of possible depth then was plotted (Fig. 2.34).

$$c_{depth,j}^{RE} = \frac{1}{n} \sum_i \left( RE_{i,j}^T - RE_{i,j}^E \right)^2; \quad (2.44)$$

$$a_{depth}^{RE} = \frac{1}{k} \sum_j c_{depth,j}^{RE}; \quad (2.45)$$

where  $RE_{i,j}^T$  and  $RE_{i,j}^E$  are theoretical and experimental relative diffraction efficiencies of  $i$ -th maxima at  $j$ -th illumination angle,  $n$  is number of measured maxima and  $k$  is number of illumination angles.

One can see that  $c_{depth,j}^{RE} = f(h)$  is a periodical function, i.e. direct comparison of simulation results of relative diffraction efficiency and experimental relative diffraction efficiency in the case of one wavelength enables us to define depth of the grooves with some period only. To avoid this uncertainty multiple wavelengths were used in this case. Comparing experimental values of relative diffraction efficiency of 5 diffraction maxima ( $\pm 2, \pm 1, 0$ ) for three different wavelengths and corresponding theoretical relative diffraction efficiencies, the depth of the channels



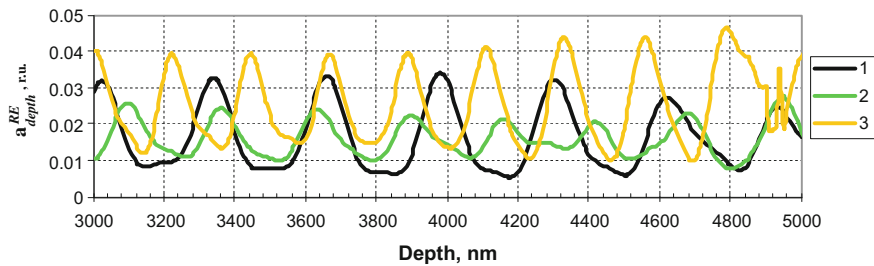


**Fig. 2.34** Average sum of squared differences between simulated and experimentally measured relative diffraction efficiencies for different wavelengths lasers versus depth of the rectangular phase reflection diffraction gratings produced in silicon: 1–632.8; 2–532; 3–441.6 nm

was defined as a minimum of the average of  $a_{depth}^{RE} = f(h)$  for all three different wavelengths. According to Fig. 2.34 this minimum is in the vicinity of 3790 nm.

Results obtained in the first approach were compared with the calculations made using the second approach. In this case three functions  $a_{depth}^{R-G} = f(h)$ ,  $a_{depth}^{R-B} = f(h)$  and  $a_{depth}^{G-B} = f(h)$  defined according to Eqs. (2.46)–(2.48) were plotted as function of depth of grooves as it shown in Fig. 2.35.

$$a_{depth}^{R-G} = \frac{1}{k} \sum_j \left( RD_{R-G,j}^T - RD_{R-G,j}^E \right)^2 \quad (2.46)$$

$$a_{depth}^{R-B} = \frac{1}{k} \sum_j \left( RD_{R-B,j}^T - RD_{R-B,j}^E \right)^2 \quad (2.47)$$

$$a_{depth}^{G-B} = \frac{1}{k} \sum_j \left( RD_{G-B,j}^T - RD_{G-B,j}^E \right)^2 \quad (2.48)$$

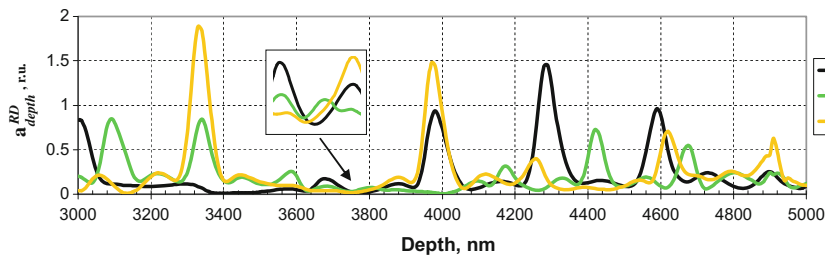


**Fig. 2.35** Average sum of squared differences between simulated and experimentally measured distances of relative diffraction efficiencies for different wavelengths lasers versus depth of the rectangular phase reflection diffraction gratings produced in silicon: 1— $a_{depth}^{R-G}$ , 2— $a_{depth}^{G-B}$ , 3— $a_{depth}^{R-B}$

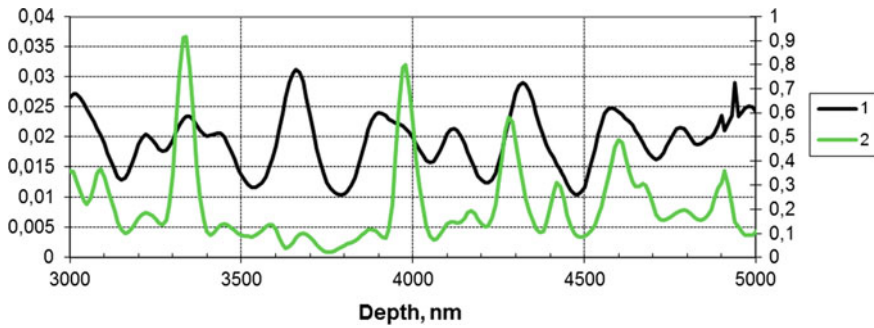


**Fig. 2.36** Average curves of  $a_{depth}^{RE}$  (1) and  $a_{depth}^{RD}$  (2) versus depth of the rectangular phase reflection diffraction gratings produced in silicon

Comparing experimental values of relative differences between the zero order relative diffraction efficiencies maxima measured with three different wavelengths and corresponding theoretical relative diffraction efficiencies, the depth of the channels was defined as a minimum of all three curves  $a_{depth}^{R-G}$ ,  $a_{depth}^{G-B}$ ,  $a_{depth}^{R-B}$  (Fig. 2.35) for different wavelengths (632.8, 532 and 441.6 nm) in the vicinity of 3760 nm. The depth of grooves of microstructures can be specified from the minima of average curves  $a_{depth}^{DE}$  and  $a_{depth}^{RD}$  (Fig. 2.36). It was found that the depth is equal to 3775 nm.

This range of depths (3760–3790 nm) is in good agreement with the results of SEM analysis demonstrating feasibility of the proposed method. Contrary to the direct method (SEM or AFM) the proposed analysis combining computer simulation and experimental results of relative diffraction efficiency versus different angle of incidence and wavelength of employed light can be used for in situ analysis e.g. control of kinetics of microfluidic device.

## 2.3 Polycarbonate as an Elasto-Plastic Material Model for Simulation of the Microstructure Hot Imprint Process

### 2.3.1 Theoretical Background for Finite Element Model of Hot Imprint Process

The aim of the hot imprint model is to help the pattern and mold designer predict the main flat imprint parameters, namely, the loads, temperature and velocity fields, the overall geometric changes of deformed pieces, as well as the optimum conditions for the flat imprint process.

Stoyanov et al. [25] in nano-imprint forming (NIF) process used four steps:

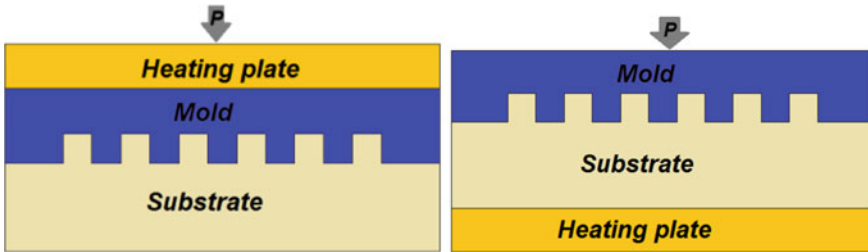


**Fig. 2.37** Schematic imprint process diagram with one heating plate

1. Softening of a thin film of formable material deposited on a substrate;
2. Pressing a rigid mould which has the required (negative) pattern of features onto the formable material;
3. Curing the formable material by cooling down to temperature below glass transition temperature ( $T_g$ );
4. Releasing the mold.

Depending from tool which is used in experiment, hot embossing process model have one or two heating plates (Figs. 2.37 and 2.38).

Some researches in the modeling and simulation of hot embossing process use three steps. Depending from requirements of the model and expected results, they integrate two steps in one, how heating and imprint, cooling and demolding. It is possible, when created model conform expected and predicted results, and is adequate by experimental date. He et al. [27] in hot imprint process modeling used three steps: molding (include preheating), cooling, demolding.

Typical hot imprint process is shown in Fig. 2.39. Black line represents changes of temperature and dotted line—pressure. In hot embossing process, a thermoplastic polymer is heated over or near its glass transition temperature ( $T_g$ ), and a fine mold is pressed into the polymer. After cooling down below  $T_g$  with pressure, the mold is released and the fine pattern on the mold is transferred to the polymer.

**Fig. 2.38** Schematic imprint process diagram with two heating plates

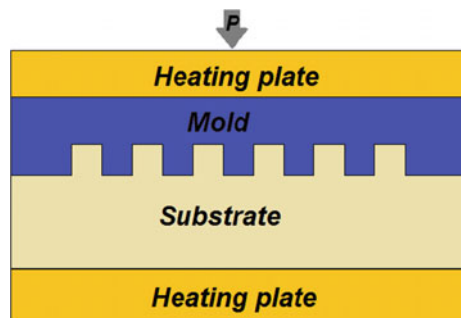
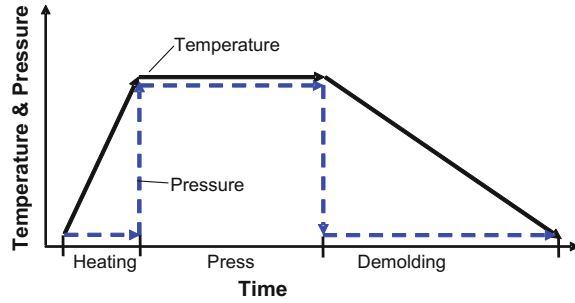


**Fig. 2.39** Typical hot imprint process



Especially in hot imprint process, cycle time is a very important issue. Substrate temperature is rising depending on the time during the heating process (Fig. 2.39). In this process there is no pressure, it equals 0. At the beginning of the second step, pressure is applied in the mold and it stays constant to the end as temperature. At the beginning of the step three, the mold is removed. It means that pressure becomes 0 and temperature of the substrate decreases. Velocity of temperatures decreasing depends from materials and environment.

Some researches simulated and analyzed just one of the hot imprint process steps. Lan et al. [28] analyzed imprint step and filling ratio at different temperature and imprinting time. Song and et al. [29] analyzed only demolding step in thermal imprint lithography. Anyway, the model could be used for detail analysis when it corresponds the experimental results.

Hot imprint process can be performed isothermally and non-isothermally. The isothermal hot imprint means the substrate and mold will be heated to the same temperature during imprint process. The non-isothermal imprints means that the mold and substrate will be heated to different temperature [30]. Isothermal method is the most popular process for the hot embossing of solid polymers. The “solid polymer” refers to the polymer under glassy state and hyperelastic state [31].

Jeong et al. [32] and Juang [26] used isothermal nonlinearity conditions. Juang [26], Yao et al. [33] created nonisothermal hot embossing model. For thick polymer substrates (e.g. 2 mm), nonisothermal embossing is desired to minimize the subsequent cooling time.

Depending on the material properties, imprint temperature, solved problems many mathematical material models are created. Polymers, depending on the temperature can be classified into three states: glass, semi-molten, flow [34]. The temperature range is an answer, which material model will be use considered in the model. Developing a mathematical model, often material properties and parameters are unknown, so the researches used the experimental results.

The researchers used different material models: hyperelastic, viscoelastic, viscoplastic, elastoplastic, visco-elastic-plastic and etc.

Schmid and Carley [35], Day et al. [36] used the hyperelastic model to simulate polymer material properties in the semi-molten state. They indicated that in

semi-molten state  $T_g < T < T_g + 60$  (where  $T_g$  is the glass transition temperature) some amorphous polymer had rubber-like properties.

Krishnaswamy et al. [37] used viscoelastic and viscoplastic models, to simulate the material properties of a ductile crystalline polymer, such as polyethylene (PE), at room temperature.

Lin et al. [38] used nonlinear viscoelastic material model for PMMA, where Young's modulus, thermo-conductivity coefficient and viscosity are depended on temperature, pressure and working time. Nicoli [39] developed a continuum-mechanical constitutive theory aimed to fill the transition state from a visco-elasto-plastic solid-like to a fluid-like response. In Kiew et al. [40] model, the PMMA has elastic-plastic property under 120 °C and viscoelastic property when temperature exceeds 120 °C. This means that PMMA will remain in the solid state when temperature is below 120° and semi-molten state when temperature is above 120 °C. Kim et al. [41] analyzed thermal NIL process using the viscoelastic material model for PMMA with a temperature range  $T_g < T < T_g + 40$ . Yao et al. [33] used viscoplastic material model for PMMA and solved the coupled flow and heat transfer problem in the nonisothermal embossing process. Jin et al. [42] used combination of two models: non-Newtonian fluid and linear-elastic solid above the glass transition temperature. Hirai et al. [43] applied the Moony-Rivlin model to understand the deformation process of polymer in the nanoimprint process. Young [44], Juang et al. [26] simulated PMMA as viscous fluid model over it glass transition temperature. Yao et al. [33] simulated non-isothermal hot embossing process for PMMA as viscoplastic flow material model. They indicated flow movement and temperature distribution inside the cavity for different cavity thickness. Song et al. [29] used viscoelastic material model for the thermal imprint lithography simulation. Dupaix and Cash [45] created a hyperelastic-viscoplastic constitutive model for amorphous polymer for hot embossing process.

There are a few hot imprint models for polycarbonate (PC). Lan et al. [28] obtained a numerical viscoelastic material model based on generalized Maxwell model for the material near the glass transition temperature ( $T_g$ ) for PC. A number of preliminary tensile stress relaxation tests were carried out at 150 °C at different instantaneous strain to produced stress relaxation curves. These curves were used to estimate model parameters. Kiew et al. [40] converted temperature-stress-strain experimental data points into a matrix expression and got the full scale deformation trend. This method helps the process engineers to gain insights on how the polymer substrate would behave during the hot imprint process. Lin et al. [38] did uniaxial compression experiments at various temperatures and creep test in order to obtain required material parameters for viscoelastic model. The stress/strain data from the compression test was used to specify the short-term elastic properties, i.e. handles the instantaneous displacement behavior of the PMMA during the situation of loading and unloading. The shear stress relaxation modulus from the creep test was used to specify the time-dependent behavior of PMMA.

The hot imprint process can be modeled as a two-dimensional or a three-dimensional problem. Both have their advantages and trade-offs. The 3-D

model is more accurate in its description of the process because it takes into account the spread (deformation in the direction of the thickness) that the work piece undergoes. This important factor is ignored by the 2-D plane strain models where  $\varepsilon_z = 0$ . The 3-D method is however more computationally expensive as the number of elements is increased. One of the most efficient approaches to the simulation of the flat imprint process is the plane-strain method. 2D model and simulation reduce the computing time and computer recourses.

Many researchers are used simplified a two-dimensional plain strain model [28, 31, 33, 40]. A small fillet was made on the mold, so as to avoid some impractical damage of the elements, such as molds penetrate through the element [31, 33, 40] (Fig. 2.40).

If the pattern of the mold is regular and symmetric just part of the mold with symmetric boundary conditions could be used for simulation [28]. Some researches are used in hot imprint process concave and convex mold type [30].

The success and efficiency of a nonlinear material solution depends on the choice of material model. Even the most complex material models are still significant idealizations of the real situation. The material nonlinearities in the hot imprint process are due to the high degree of plasticity. The plastic behavior is defined the following:

**Yield Criteria:** when plastic behavior is expected need tell the solver which criteria to seek to initiate yielding. The transition from elastic to the plastic state occurs when the stress reaches the yield point of the material. Yield criteria are a function of the stresses in the model.

The von Mises yield criterion given by the alternative forms of equation

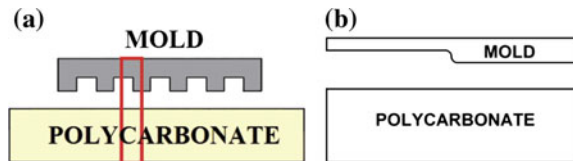
$$\bar{\sigma} = f(\sigma_{ij}) = \sqrt{\frac{1}{2}(\sigma_x - \sigma_y)^2 + (\sigma_y - \sigma_z)^2 + (\sigma_z - \sigma_x)^2 + 6(\tau_{xy}^2 + \tau_{yz}^2 + \tau_{zx}^2)} = \sigma_Y, \quad (2.49)$$

$$\bar{\sigma} = f(\sigma_{ij}) = \sqrt{(\sigma_1 - \sigma_2)^2 + (\sigma_2 - \sigma_3)^2 + (\sigma_3 - \sigma_1)^2} = \sigma_Y, \quad (2.50)$$

$$\bar{\sigma} = f(\sigma_{ij}) = \sqrt{J_2} = \sqrt{s_1^2 + s_2^2 + s_3^2} = \frac{1}{2}s_{ij}s_{ij} = \frac{\sigma_Y^2}{3}, \quad (2.51)$$

and it says “yield occurs when the equivalent stress (Mises stress) equals the yield stress in uniaxial tension  $\sigma_Y$ , i.e.,  $\bar{\sigma} = \sigma_Y$ ”,  $s_{ij}$ —components of the deviatoric stress tensor [46–48].

**Fig. 2.40** Micro thermal imprint process and its analytical model: **a** schematic diagram of imprint process, and **b** simplified plain strain analytical model



The yield surface,  $F$ , for the Drucker-Prager material law is given by

$$F = \alpha I_1 + \sqrt{J_2} = K, \quad (2.52)$$

where  $I_1$  is the first stress invariant and  $J_2$  is the second deviatoric stress invariant.

The first stress invariant is defined using the normal stress components:

$$I_1 = \sigma_x + \sigma_y + \sigma_z. \quad (2.53)$$

The second stress invariant is defined by

$$I_2 = \sigma_x \sigma_y + \sigma_y \sigma_z + \sigma_z \sigma_x - \tau_{xy}^2. \quad (2.54)$$

The second deviatoric stress invariant can be expressed using the first and the second stress invariants:

$$J_2 = \frac{1}{3} I_1^2 - I_2. \quad (2.55)$$

If two-dimensional plane-strain conditions prevail, the Drucker-Prager criterion becomes identical to the Mohr-Coulomb criterion if the material parameters  $\alpha$  and  $K$  are given by

$$\alpha = \frac{\tan \phi}{\sqrt{9 + 12 \tan^2 \phi}}, \quad (2.56)$$

$$K = \frac{3c}{\sqrt{9 + 12 \tan^2 \phi}}, \quad (2.57)$$

where  $c$  is cohesion value,  $\phi$ —angle of internal friction [49].

**Hardening Rule:** determines the material model responds to repeated stress reversals. The yield point in tension can be expected to be equal to the opposite of the yield stress in compression.

An Isotropic hardening the compressive yield always equals the tensile yield: the absolute value defined yield stress.

In order to derive the formula for hardening, total effective strain is given as

$$\varepsilon_{eff} = \varepsilon_{ep} + \frac{\sigma}{E}, \quad (2.58)$$

where  $\varepsilon_{eff}$  is the effective strain and  $\varepsilon_{ep}$  is the effective plastic strain. Then hardening criterion is given

$$\sigma_{hard} = \sigma_{exp}(\varepsilon_{eff}) - \sigma_Y = \sigma_{exp}\left(\varepsilon_{ep} + \frac{\sigma}{E}\right). \quad (2.59)$$

A kinematic hardening model will take into account the reduction in the compressive yield point after a stress reversal. Kinematic hardening is said to take place (Fig. 2.41). It is frequently observed in experiments that, after being loaded (and hardened) in one direction, many materials show a decreased resistance to plastic yielding in the opposite direction [50]. This phenomenon is known as the Bauschinger effect.

The evolution of a kinematically hardening von Mises-type yield surface (in the deviatoric plane) used to model the phenomenon is shown. The yield function for the kinematically hardening model is given by

$$\Phi(\sigma, \beta) = \sqrt{3J_2(\eta(\sigma, \beta))} - \sigma_y, \quad (2.60)$$

where

$$\eta(\sigma, \beta) = s(\sigma) - \beta \quad (2.61)$$

is the relative stress tensor, defined as the difference between the stress deviator and the symmetric deviatoric (stress-like) tensor,  $\beta$ , known as the back-stress tensor. The back-stress tensor is the thermodynamical force associated with kinematic hardening and represents the translation of the yield surface in the space of stresses. The constant  $\sigma_y$  defines the radius of the yield surface [49].

Flow rule: establishes the incremental stress-strain relations for plastic material. The flow rule describes differential changes in the plastic strain components as a function of the current stress state.

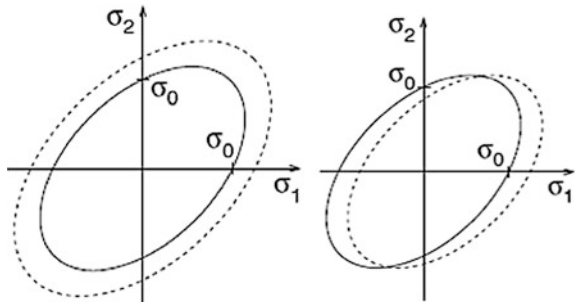
By the Prandtl-Reuss flow rule (used for elastic plastic solid formulation) is given as

$$\dot{\epsilon}_{ij}^p = \dot{\lambda} \frac{\partial f(\sigma_{ij})}{\partial \sigma_{ij}} = \dot{\lambda} s_{ij}, \quad (2.62)$$

$$\dot{\lambda} = \frac{1}{\tau_Y} \sqrt{\frac{1}{2} \dot{\epsilon}_{ij} \dot{\epsilon}_{ij}}, \quad (2.63)$$

where  $s_{ij}$ —components of the deviatoric stress tensor,  $\dot{\epsilon}_{ij}$ —components of the strain rate tensor,  $\dot{\epsilon}_{ij}^p$ —components of the plastic strain rate tensor,  $\dot{\lambda}$ —flow rule non-negative factor of proportionality,  $f(\sigma_{ij})$ —Yield function,  $\tau_Y$ —yield strength.

**Fig. 2.41** Elasto-plastic hardening models: *left* isotropic, *right* kinematic [51]





Geometric nonlinearities in the hot imprint process are due to the existence of large strains and deformations. Contact and friction problems lead to nonlinear boundary conditions. This type of nonlinearity manifests itself in several real life situations; for example, metal forming, gears, interference of mechanical components, pneumatic tire contact, and crash [52].

For the following reasons, as the specifics of the model, it is necessary to solve nonlinear deformable body of large displacements, heat transfer and contact problems.

Strain-Displacement equations describe the basic relations between displacement and strain, which are shown as Eqs. (2.64)–(2.69).

$$\varepsilon_x = \frac{\partial u}{\partial x} \quad (2.64)$$

$$\varepsilon_y = \frac{\partial v}{\partial y} \quad (2.65)$$

$$\varepsilon_z = \frac{\partial w}{\partial z} \quad (2.66)$$

$$\gamma_{xy} = \frac{1}{2} \left( \frac{\partial u}{\partial y} + \frac{\partial v}{\partial x} \right) \quad (2.67)$$

$$\gamma_{yz} = \frac{1}{2} \left( \frac{\partial w}{\partial y} + \frac{\partial v}{\partial z} \right) \quad (2.68)$$

$$\gamma_{zx} = \frac{1}{2} \left( \frac{\partial u}{\partial z} + \frac{\partial w}{\partial x} \right) \quad (2.69)$$

Here  $\varepsilon_x, \varepsilon_y, \varepsilon_z, \gamma_{yz}, \gamma_{xz}, \gamma_{xy}$  are linear deformation by x, y, z direction and shear deformations on yz, xz, xy plane, u, v, w—displacements by x, y, z direction.

Strain compatibility equation is based on the consideration of the continuum assumption. When we analyze the strain-displacement behavior of a small 3-D element, we must ensure the continuity of material before and after deformation. Equations (2.70)–(2.75) are first derived by Saint-Venant from the strain-displacement equation.

$$\frac{\partial^2 \varepsilon_x}{\partial y^2} + \frac{\partial^2 \varepsilon_y}{\partial x^2} = \frac{\partial^2 \gamma_{xy}}{\partial x \partial y} \quad (2.70)$$

$$\frac{\partial^2 \varepsilon_y}{\partial z^2} + \frac{\partial^2 \varepsilon_z}{\partial y^2} = \frac{\partial^2 \gamma_{yz}}{\partial y \partial z} \quad (2.71)$$

$$\frac{\partial^2 \varepsilon_x}{\partial z^2} + \frac{\partial^2 \varepsilon_z}{\partial x^2} = \frac{\partial^2 \gamma_{xz}}{\partial x \partial z} \quad (2.72)$$

$$2 \frac{\partial^2 \varepsilon_x}{\partial y \partial z} = \frac{\partial}{\partial x} \left( -\frac{\partial \gamma_{yz}}{\partial x} + \frac{\partial \gamma_{xz}}{\partial y} + \frac{\partial \gamma_{xy}}{\partial z} \right) \quad (2.73)$$

$$2 \frac{\partial^2 \varepsilon_y}{\partial x \partial z} = \frac{\partial}{\partial y} \left( \frac{\partial \gamma_{yz}}{\partial x} - \frac{\partial \gamma_{xz}}{\partial y} + \frac{\partial \gamma_{xy}}{\partial z} \right) \quad (2.74)$$

$$2 \frac{\partial^2 \varepsilon_z}{\partial x \partial y} = \frac{\partial}{\partial z} \left( \frac{\partial \gamma_{yz}}{\partial x} + \frac{\partial \gamma_{xz}}{\partial y} - \frac{\partial \gamma_{xy}}{\partial z} \right) \quad (2.75)$$

In summary, to obtain the stress distribution by finite element method (FEM), firstly the force load is transferred to strain load, then displacement load by constitutive equation and strain-displacement equation, respectively. Then, the continuity equations and strain compatibility equations are solved by finite element method (convert differential equation to linear equation group) and calculate the displacement for each element. Finally, the strain and stress for each element are derived from displacement data by strain-displacement equation and constitutive equation in sequence [29].

Different processes of heat transfer can take place in one or more of the following methods: thermal conduction, convection and radiation.

In hot imprint process, on top of the material and mold, there is additional heat loss to the environment due to radiation and convection, heat loss by conduction to the mold, and temperature change.

Heat transfer conductivity is described according to the formula:

$$\rho(T)c_p(T) \frac{\partial T}{\partial t} + \nabla(-k \nabla T) = q, \quad (2.76)$$

where  $k$ —thermal conductivity,  $\rho$ —density,  $c_p$ —heat capacity,  $T$ —temperature,  $q$ —rate of the heat generation.

Contact is a non-linear boundary value problem. During contact, mechanical loads and sometimes heat are transmitted across the area of contact. If friction is present, shear forces are also transmitted.

Boundary contact conditions cause huge difficulties and make the convergence of the model extremely difficult. It is necessary to match the initial geometric shape as well as possible, but also to introduce test to determine when a node comes into contact with a rigid or elastic tool. This can be done geometrically, and the node then restored to the surface if it has apparently crossed the boundary. It is then necessary to determine whether the normal force has become tensile, before re-sitting the node [52, 53].

Comsol Multiphysics realized that the contact interaction forms: node to node, node to surface, surface to surface. FEM analysis is preferred that the surface of the deformable body share a common node with the rigid body.

When modeling contact, structural parts that come into contact have to be defined and consisted of two sets of boundaries, a slave and a master domain. The slave boundaries can't penetrate the master boundaries [54].

Describing of the contact, the polymer is as deformable body, that mechanical characteristics of the parameters is much little than the rigid body. Simulation assumed that the solid body is non-penetrated.

COMSOL Multiphysics solves contact problems using augmented Lagrangian method. This method is a combination of penalty and Lagrange multiplier methods. It means a penalty method with penetration control. The system is solved by iteration from the determined displacement. These displacements caused by incremental loading, are stored and used to deform the structure to its current geometry. If the gap distance between the slave and master boundaries at a given equilibrium iteration is becoming negative, (the master boundary is penetrating the slave boundary), the user defined normal penalty factor  $p_n$  is augmented with Lagrange multipliers for contact pressure  $T_n$

$$T_{np} = \begin{cases} T_n - p_n g & \text{if } g \leq 0 \\ T_n e^{-\frac{p_n g}{T_n}} & \text{otherwise} \end{cases}, \quad (2.77)$$

$g$  is the gap distance variable between slave and master boundary [54, 55].

Polymers can be classified in standard polymers, technical polymers and high performance polymers, according to their temperature stability. The group of thermoplastic polymers is split into the groups of amorphous and semicrystalline polymers. Further the thermoplastic polymers can be modified with certain fillers in the micro and nano range to improve the mechanical stability and to reduce anisotropic behaviour in the molded part. Here the size and the shape of the filler in comparison to the size of the microcavities will limit the use of filled polymers.

Amorphous polymers like PMMA and PC are well suited in thermal imprint process because of their molecular structure [34]. It is known that the material property of amorphous polymer is strongly dependent on the conditions, such as temperature and loading. The material deformation behavior of amorphous polymer resists is a function of temperature can be classified into three states: glassy state, rubbery state and flow state [41]. When the temperature is lower than the glass transition temperature  $T_g$ , it is glassy state, in which amorphous polymer acts like a hard and brittle solid glass. The deformation is reversible. As the temperature is increased, it goes to a rubbery state, in which the polymer acts like an incompressible or approximately incompressible rubber. From glassy state to rubbery state there is no strict temperature, "jumping point", however, there is a transition region. The temperature range of this transition region is from 5 to 20 °C, depending on the characteristic of the polymer [56]. From the transition region to the rubbery state, the polymer shows dual response of reversible and irreversible deformation for mechanical stress. This property is regarded as the so-called viscoelasticity. When the temperature is further increased, it goes to the flow state, in which the polymer melts and can be regarded as a viscous non-newtonian liquid. The material deformation is irreversible [41, 47].

2.3.2 Finite Element Model of Hot Imprint Process

The mathematical model of the process of mechanical hot imprint into polycarbonate near it’s glass transition temperature is presented in this chapter. Experimental results were compared with hot imprint simulations in order to investigate the effectiveness of the new model. These simulations help better to understand the mechanical hot imprint process. The modelling and simulation methodology by FEM including geometrical modeling, boundary conditions, meshing, material properties, process conditions and governing equations are presented. FE model was created using Comsol Multiphysics software.

Hot imprint model creation diagram is shown in Fig. 2.42. The equations of motion, thermal balance, material properties and material deformations were used to calculate stress, strain, temperature fields, distribution of mold pressure and filling ratio in each step of the hot imprint process.

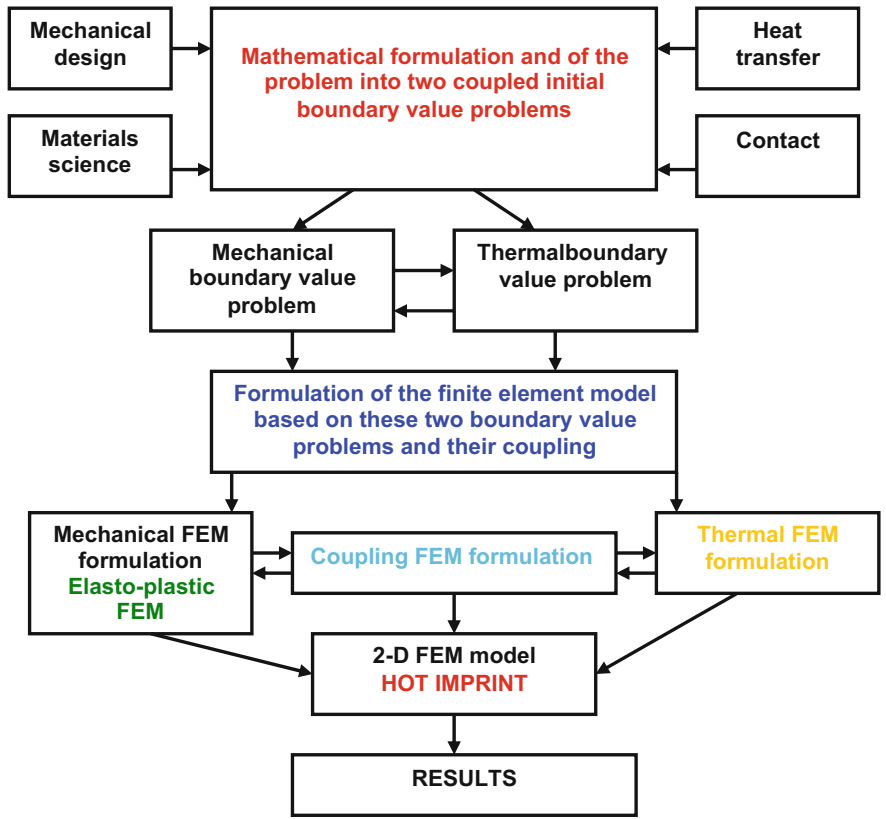


Fig. 2.42 Diagram of creation of the hot imprint FE model

As discussed in the Sect. 2.3.1 most of the authors of scientific papers divide mechanical hot imprint process into four major steps:

- 1. Preheating;
- 2. Imprint;
- 3. Cooling;
- 4. Demolding.

In this modeling (Fig. 2.42) the elasto-plastic material model was chosen. This model is simplified by assuming, that polycarbonate can be cooled in a very short period of time, thus a separate cooling step is not analyzed.

In Sect. 2.3.1 analyzed dependence between temperature and pressure from time is modified for this model as shown in Fig. 2.43. This model consists from three steps: heating, imprinting and demolding (Fig. 2.44).

Although many periodical nanometer-scale patterns are defined on the mold, it is impractical to consider all of them using the FEA. If the cross-sectional shape of the mold is constant in one direction, as in the line pattern shown in Fig. 2.45,

**Fig. 2.43** Diagram of mechanical hot imprint process

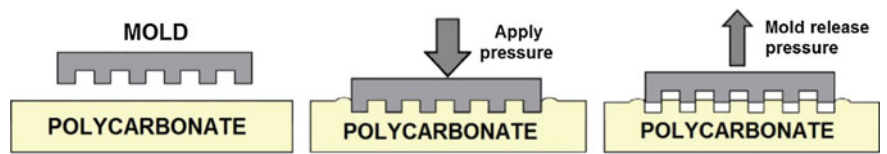
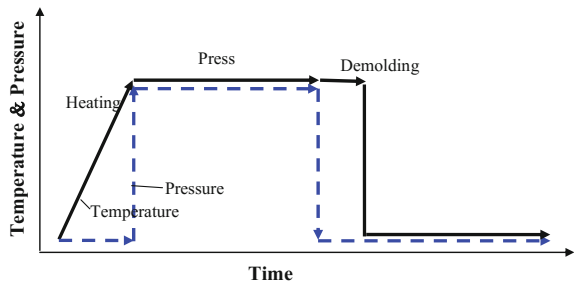


**Fig. 2.44** Steps of mechanical hot imprint process of periodical microstructure: *left* heating step; *middle* hot imprint step; *right* demolding step

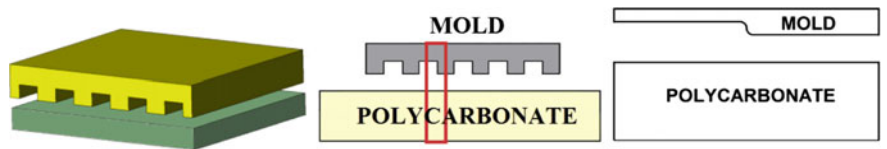


**Fig. 2.45** Geometry of the hot imprint model: *left* 3D model; *middle* 2D model; *right* parts of 2D mode

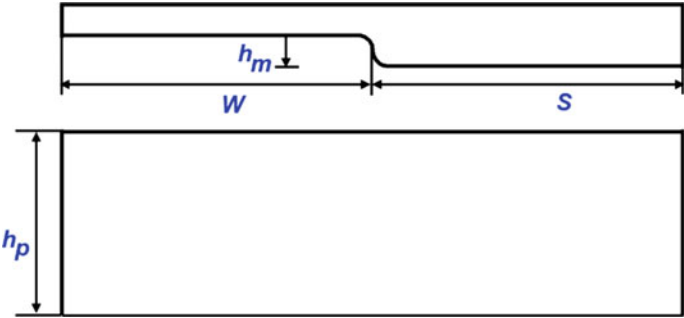


**Fig. 2.46** Geometrical parameters of the microstructure model

**Table 2.3** Model’s geometrical parameters

Parameters	Value
$h_m$ —depth of the mold	100 nm
$h_p$ —thickness of the polycarbonate	3 mm
$2W$ —length of the cavity	2 $\mu\text{m}$
$2S$ —length of the ridge	2 $\mu\text{m}$

two-dimensional stress analysis is possible. Moreover, if the offset and recessed pattern of the mold is regular and symmetric, we can assume a two-dimensional plane strain model of a unit cell of the patterned mold using FE analysis model by taking into account symmetric boundary conditions (Fig. 2.46 and Table 2.3). To avoid stress concentration in a finite element node, a small radius was made in the corner of the mold.

The complete simulation requires two analytical models: thermal analysis, using the heat transfer module and mechanical analysis, using module of structural mechanics together with data and solutions. The boundary conditions and initial values in Comsol Multiphysics software are described in three levels: sub-domains, edges and points. Figure 2.47 shows two-dimensional (2-D) FEM model of a Nickel mold, Polycarbonate substrate and boundary conditions.

Plain strain was chosen for analysis. The mold is made of more rigid material than the polycarbonate, thus it was assumed that the mold has rigid contact surfaces in FE simulation. Symmetric boundaries were used on two sides of the model. A symmetric boundary indicates that displacement and temperature gradients across the boundary are equal to zero. Fixed normal displacement was applied to the bottom surface of the substrate. Thermal boundary and fixed normal displacement were used in order to approximate mechanical and thermal boundaries of the portion of polycarbonate’s surface to the side of cavity (the thickness of the polycarbonate is much larger than thickness of cavity). Arc of small radius between mold’s A and B areas is formed, in order to improve the convergence of the simulation. The initial temperatures of mold and polycarbonate are 293 K. Mold’s temperature  $T = f(T, t)$  is defined as function of mold’s heating temperature  $T$  (Kelvin) and time  $t$  (seconds) (Fig. 2.48, Tables 2.4 and 2.5).

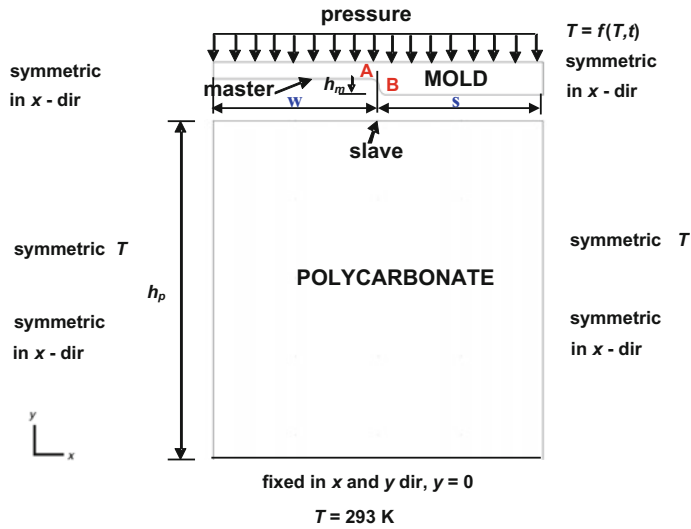


Fig. 2.47 Boundary conditions of the hot imprint process

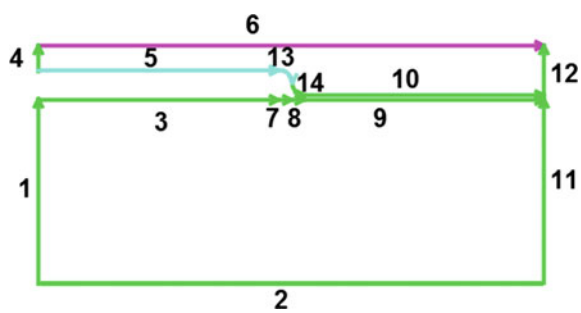


Fig. 2.48 Models edges numeration

Table 2.4 Mechanical boundary conditions

Constrain		
Symmetry plane	Free	Prescribed displacement
1, 4, 11, 12	3, 5, 7, 8, 9, 10, 13, 14	$x = 0, y = 0$ 2, $x = 0, y = y(t)$ 6

Table 2.5 Thermal boundary conditions

Thermal boundary conditions			
Insulation/symmetry $-n(-k\nabla T) = 0$	Temperature $T = T_0$	Temperature $T = f(T_s(t))$	Convective flux $-n(-k\nabla T) = 0$
1, 11	2	4, 5, 6, 10, 12, 13, 14	3, 7, 8, 9

**Table 2.6** Contact pairs

Master	Slave
5, 10, 13, 14	3, 7, 8, 9

The mathematical model for heat transfer by conduction is expressed by the heat equation:

$$\rho c_p \frac{\partial T}{\partial t} - \nabla(k \nabla T) = 0, \quad (2.78)$$

where  $k$ —thermal conductivity,  $\rho$ —density,  $c_p$ —heat capacity,  $T$ —temperature.

In order to obtain the solution for stress, strain, rate of strain, velocity and temperature fields within the imprinted polycarbonate, appropriate boundary and initial conditions must be defined.

The contact's type in this model is rigid-deformable. The mold is rigid body (master) and polycarbonate—deformable body (slave). Since the model is a 2-D, contact boundary conditions are described in pairs of contact edges Table 2.6.

Materials, used for the mold and substrate, together with their properties are listed in Table 2.7. Nickel was used as a mold material, and it was assumed to be isotropic and elastic. The material, used as substrate, was polycarbonate. It is amorphous polymer with a glass transition temperature of about 423 K.

Simulation of hot imprint process using coupled time-depend thermo-mechanical analysis is presented in diagram (Fig. 2.49). It includes heat transfer, structural mechanics and contact analysis. Also it takes into account all necessary material parameters such as thermal conductivity ( $k$  in W/mK), density ( $\rho$  in kg/m<sup>3</sup>), heat capacity ( $c_p$  in J/kg K), Young's modulus ( $E$  in N/m<sup>2</sup>), Poisson's ratio ( $\nu$ ) and thermal expansion coefficient ( $\alpha$  in K<sup>-1</sup>), which is defined as function of temperature [42, 57].

Mechanical properties and material behaviour of the formable material during hot imprint process are extremely important when identifying optimal process conditions for the manufacture of defect-free nano-structures. An accurate determination of critical material parameters below or above  $T_g$  is considered as a key requirement for the numerical simulation.

**Table 2.7** Material properties of the mold and polycarbonate

	Mold	Substrate
Material	Nickel	Polycarbonate
Density, kg/m <sup>3</sup>	$8.908 \times 10^3$	$\rho(T)$
Thermal conductivity, W/m K	90.9	$k(T)$
Thermal expansion, 1/K	$13.4 \times 10^{-6}$	$6.5 \times 10^{-5}$
Heat capacity, J/kg K	445	$c_p(T)$
Elastic modulus, GPa	200	$E(T)$
Poisson's ratio	0.31	$\nu(T)$



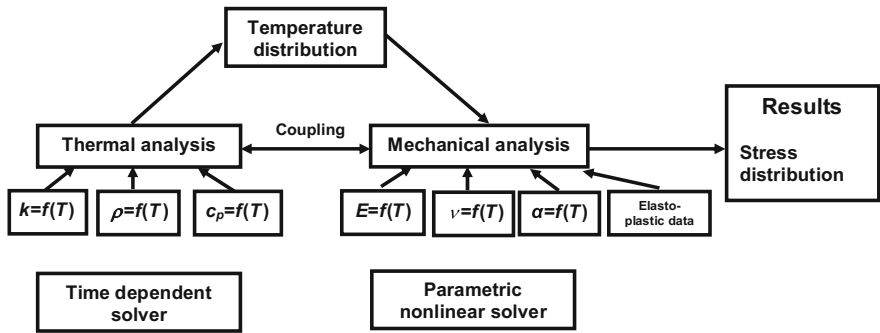


Fig. 2.49 Diagram of thermo-mechanical analysis

The following set of graphs, which is presented by Comsol Multiphysics 3.5a material library, describes the thermal conductivity, density, Poisson ratio, heat capacity and Young modulus of the polycarbonate, which is used in hot imprint process.

In Fig. 2.50 it can be seen how thermal conductivity depends on the temperature. This is an important fact for the hot imprint process. In this process PC temperature increases rapidly, this increment significantly influences on the heat transfer between the mold and the PC.

Elastic-plastic materials are employed in order to describe deformation under large strain. In this model, polycarbonate is described as elasto-plastic material.

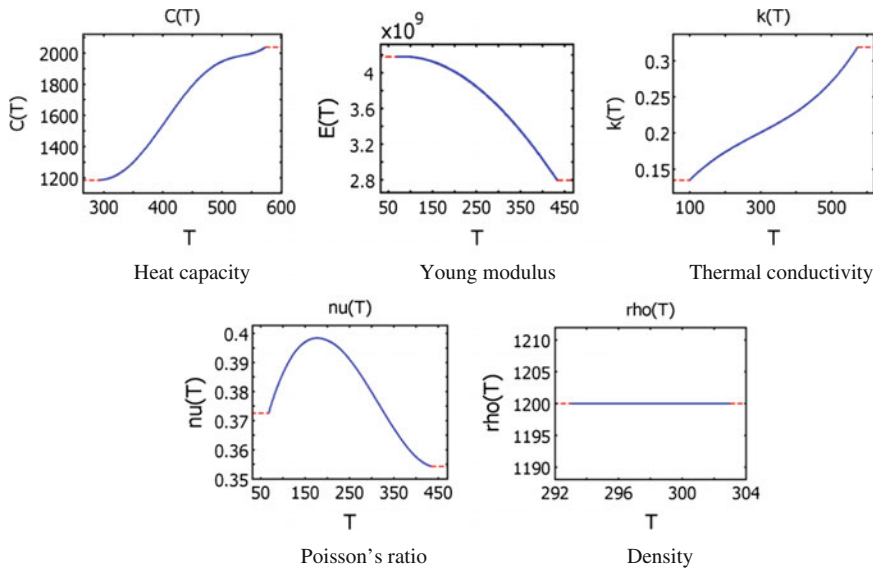


Fig. 2.50 Thermal dependencies of polycarbonate material parameters

The micro hot imprint process is being performed near the glass transition temperature of polycarbonate, at which it behaves like elasto-plastic material. Under the constant load material would undergo two stages of deformation: an instantaneous elastic deformation  $\varepsilon_e$  at the beginning of the process, followed by plastic deformation  $\varepsilon_p$ . The total deformation is described as:

$$\varepsilon = \varepsilon_e + \varepsilon_p. \quad (2.79)$$

The behaviour of elasto-plastic material can be described as a model with a set of spring and friction components. Rheological models of elasto-plastic body with hardening are given in Figs. 2.51 and 2.52, where  $\sigma_k$ —yield strength,  $E_2$ —modulus of plasticity,  $E_1$ —modulus of elasticity (Fig. 2.51).

In Fig. 2.52 means [49]:

$$\operatorname{tg} \alpha = E_1, \quad \operatorname{tg} \beta = \frac{E_1 \cdot E_2}{E_1 + E_2}. \quad (2.80)$$

Elastic-plastic models in FE systems require data in the form of elastic constants in order to describe elastic behavior and parameters, which describe yield, hardening and flow behavior in order to describe plastic behavior.

**Fig. 2.51** Schematic diagram of elasto-plastic model

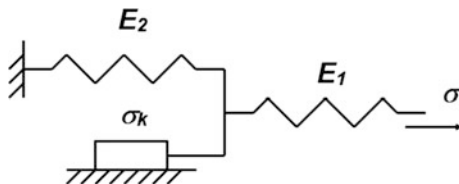
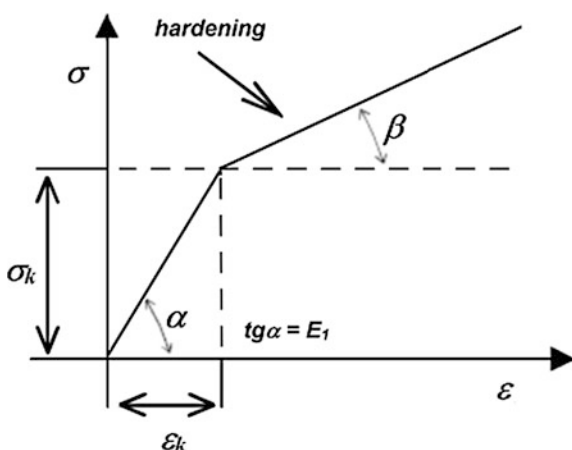


**Fig. 2.52** Deformation characteristic



In this model the yield function von Mises was used

$$\sigma_Y = \sqrt{\frac{1}{2}(\sigma_1 - \sigma_2)^2 + (\sigma_2 - \sigma_3)^2 + (\sigma_1 - \sigma_3)^2}, \quad (2.81)$$

where  $\sigma_1, \sigma_2, \sigma_3$  are principal stresses and  $\sigma_Y$  is the equivalent stress.

The yield stress level  $\sigma_{ys}$  and isotropic hardening  $E_{Tiso}$  are as a function depending on temperature:

$$\sigma_{ys} = f(T), \quad (2.82)$$

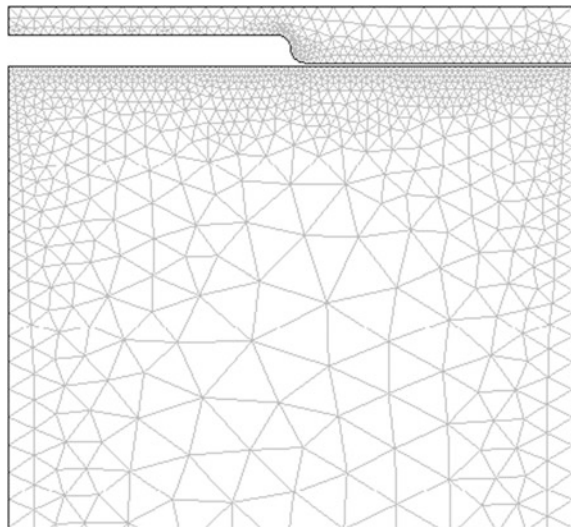
$$E_{Tiso} = g(T). \quad (2.83)$$

The hardening function is a function of the effective plastic strain and describes the behavior, which starts from the yield stress of the material.

The geometrical singularity can cause a high rate polymer deformation. The accuracy and convergence of the solution depend on the choice of the meshing. As can be seen in Fig. 2.53, the contact areas have more refined elements than those areas, which do not have contact during the deformation. Also the mesh at the symmetrical region is carefully structured and has more refined element than the rest in domain. The model consists of 5583 finite elements.

The mesh of the model, using triangle quadratic Lagrange finite elements, is presented in Fig. 2.53. It is fine in the contact between the mold and polycarbonate. Fine mesh guarantees the convergence of the solution. The triangular element is defined by six nodes, each having three degrees of freedom: displacement in the nodal horizontal  $x$  and vertical  $y$  directions, and temperature. Finite element of Lagrange-Quadratic type was chosen. This type is used for 2-D modeling of solid structures.

**Fig. 2.53** Finite element mesh



There are six nodes in this element: three corner nodes and three mid-side nodes. The displacements ( $u$ ,  $v$ ) are assumed to be quadratic functions of ( $x$ ,  $y$ ),

$$\begin{aligned} u &= b_1 + b_2x + b_3y + b_4x^2 + b_5xy + b_6y^2 \\ v &= b_7 + b_8x + b_9y + b_{10}x^2 + b_{11}xy + b_{12}y^2, \end{aligned} \quad (2.84)$$

where  $b_i$  ( $i = 1, 2, \dots, 12$ ) are constants.

Several assumptions are made in order to simplify the model. The mechanical behavior of both nickel and polycarbonate at the simulated scale is governed by the equation of continuum mechanics, in which we consider all object to be continuous. The surfaces of contacting bodies are perfectly smooth. Adhesion is neglected. The cooling step is integrated into demolding step. The contact friction coefficient is assumed to be zero at the interface between the mold and polymer. No air is trapped inside the microcavities and buckling phenomenon, due to surface tension, is ignored. Heat losses to the environment are neglected. The mold remains hot all the time.

### 2.3.3 Hot Imprint Process Simulation Results

In general, the simulation model and numerical results provide with useful understanding of the fundamental formation mechanism during the hot imprint process and serve as a useful guide for specifying the optimal processing conditions for variety of hot imprint applications.

Hot imprint process was divided into three steps: heating, imprinting and demolding. In this case:

- (1) Heating. The initial temperature of the mold and polycarbonate is 293 K (environmental temperature). When the stamp touches polycarbonate, the heating of the mold up to 421 K temperature begins. During the heating process, the heat is carried to the polycarbonate and it starts to deform due to the effect of the heat. The heating step lasts about  $t = 2 \times 10^{-7}$  s.
- (2) Imprinting. During this process, the mold goes down and presses polycarbonate, at the same time the contact force between the mold and polycarbonate increases. Polycarbonate is being further deformed and plastic deformation appears.
- (3) Demolding. In this step, the hot mold ( $T = 421$  K) is demolded and finally polycarbonate is cooled. Polycarbonate assumes the form of the mold's periodic microstructure.

The model is solved using heat transfer and solid stress-strain application modes with thermal contact problem between mold and polycarbonate. This multiphysics polycarbonate hot imprint model includes the heat transport, structural mechanical stresses and deformations, resulting from the temperature distribution. It allows

evaluate temperature distributions and stresses in the polycarbonate during hot imprint process. Obtained theoretical results were compared with experimental.

The imprint pressure is one of the main parameters and has a major impact on the quality of the replication. Insufficient pressure would result in incomplete filling of the pattern grooves and may subsequently lead to shape defect. Whereas too high imprint pressure causes high residual stresses in the polymer during the subsequent process step.

In Fig. 2.54 the dependence of imprint force from mold displacement is presented. The negative sign “-” shows that mold moves down and for analysis the absolute value is used. As shown in the graph, during the heating step the force increases slowly, this means that polycarbonate is still cold and the resistance force is high. Point A indicates the end of the heating step and from here the imprint force increases linearly up to point B—the end of imprint step. At this point the displacement of the mold is equal  $0.9 \mu\text{m}$ . From this point the demolding step starts and as can be seen from the graph the imprint force decreases linearly till the point C—end of demolding step. The changes of polycarbonate behavior in each step are presented below.

### 1. Heating step

Created model shows how polycarbonate substrate would behave under thermal load and evaluates temperature, displacement, and a stress fields during hot imprint process. As shown in Fig. 2.55, maximum Von Mises stress (107 MPa) is located in the place where the mold's corner contacts with polycarbonate during the heating process. Blank mold cavity is partially filled with heated polycarbonate. Von Mises stress in polycarbonate reaches 107.1 MPa. Temperaturational distribution of the specimen is presented in Fig. 2.55 using contour lines. Variation of temperature is in the range from 295 to 413 K.

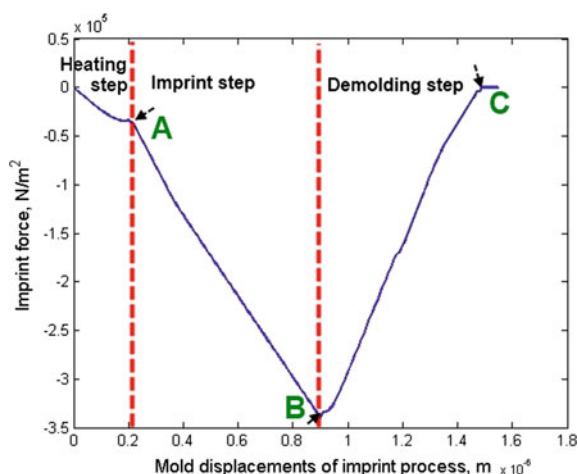
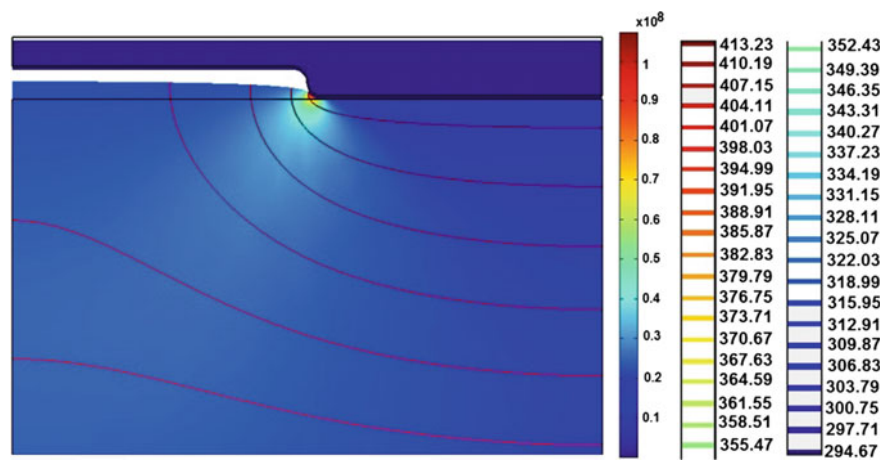
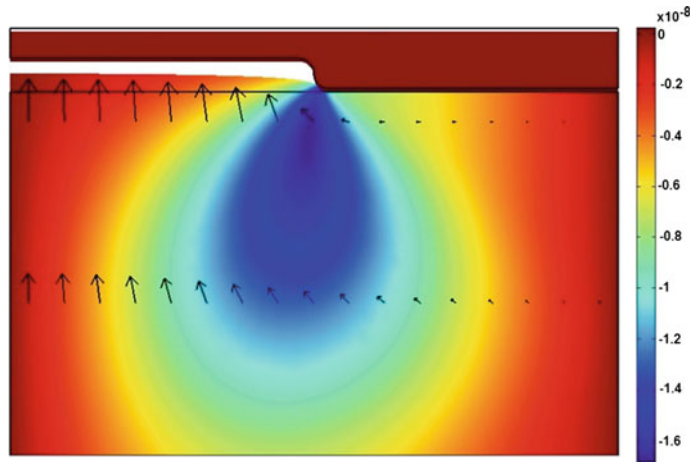


Fig. 2.54 Imprint force dependence from mold displacement



**Fig. 2.55** Von Mises stress distribution and temperature fields in the polycarbonate during heating process after  $1.9 \times 10^{-7}$  s

As shown in Fig. 2.56, maximum displacement in x direction (absolute value  $1.69 \times 10^{-8}$  m) is also located in the contact place between the mold's corner and polycarbonate. The sign “-“ means that the direction of the displacement is to left side. The arrows demonstrate the direction of total displacement. Then the mold moves down and the polycarbonate from the right side moves to the left, as shown by arrows.



**Fig. 2.56** Displacements in x direction distribution and total displacements by arrows after  $1.9 \times 10^{-7}$  s

In this model displacement in horizontal and vertical directions of the polycarbonate in contact edge (Fig. 2.57), in each hot imprint process step was analyzed. Heating process lasts only  $3 \times 10^{-7}$  s (Fig. 2.58). At the beginning of this process ( $0 < t < 1.5 \times 10^{-7}$ ) the integral displacement in x direction is equal to zero, because at this time the temperature of the polycarbonate is still near the initial temperature. The shifts of the polycarbonate were observed from  $1.5 \times 10^{-7}$  s to  $2.7 \times 10^{-7}$  s. Polycarbonate is elastic, it means, that polymer after the contact with mold areas shifts to the empty cavity of the mold. The cavity of the mold is partially filled with heated polycarbonate. At the time of  $2.7 \times 10^{-7}$  s deformations of the polycarbonate stop. It means the heating process becomes steady.

## 2. Imprinting step

After the imprinting process (Fig. 2.59) the absolute value of the largest displacement in the x direction is observed in the empty cavity of the mold and in contact place with polycarbonate. During the imprint process, the mold moves down from the initial position by approximately 710 nm. Absolute value of the polycarbonate displacement in the x direction is from 9 to 85 nm. The arrows show that total displacement after hot imprint process is diverted to down. It means, that polycarbonate moves down uniformly in all area.

As shown in Fig. 2.60, maximum Von Mises stress (344 MPa) is located in the place where the mold's corner and polycarbonate contact. Blankmold cavity is filled

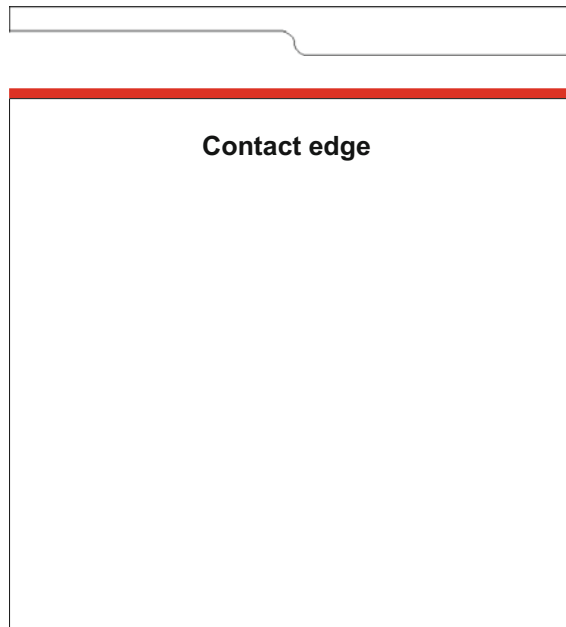


**Fig. 2.57** Contact edge in the model

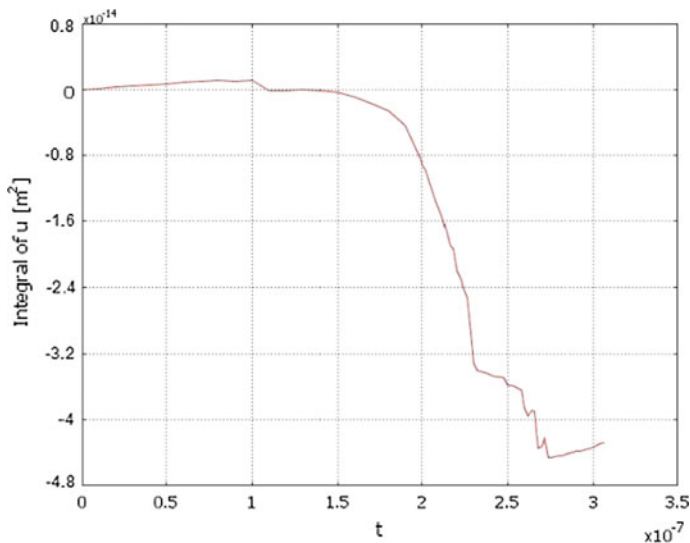


**Fig. 2.58** Integral displacement in x direction of the contact edge in heating step

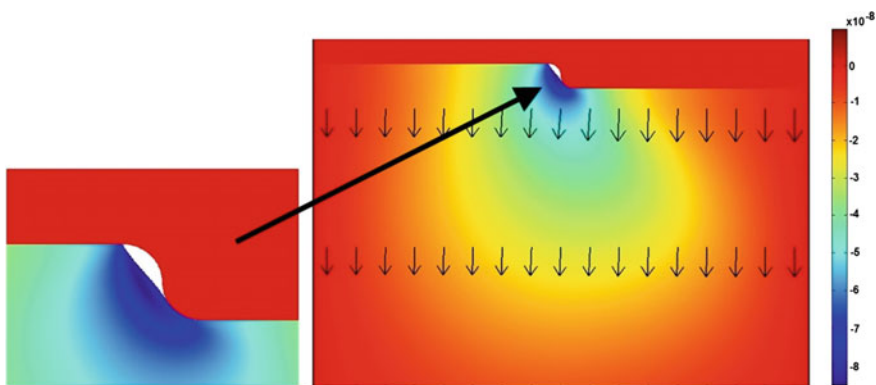


**Fig. 2.59** Deformed polycarbonate and displacement in x direction distribution and temperature fields after imprint step

with heated polycarbonate. Only small cavity remains empty. The temperature in the upper layer of the polycarbonate reaches the maximum value of 419 K. The lines of the temperature fields in the sample attain the form of the periodic microstructure. It means that there is an empty area in the mold of the polycarbonate. It appeared due to features of polycarbonate (Fig. 2.61).

During the imprint step ( $0 < t < 1.4 \times 10^{-7}$  s) the integral displacement module increases linearly in x direction (Fig. 2.6). After the imprint step an empty area remains between the mold and polycarbonate (Fig. 2.59).



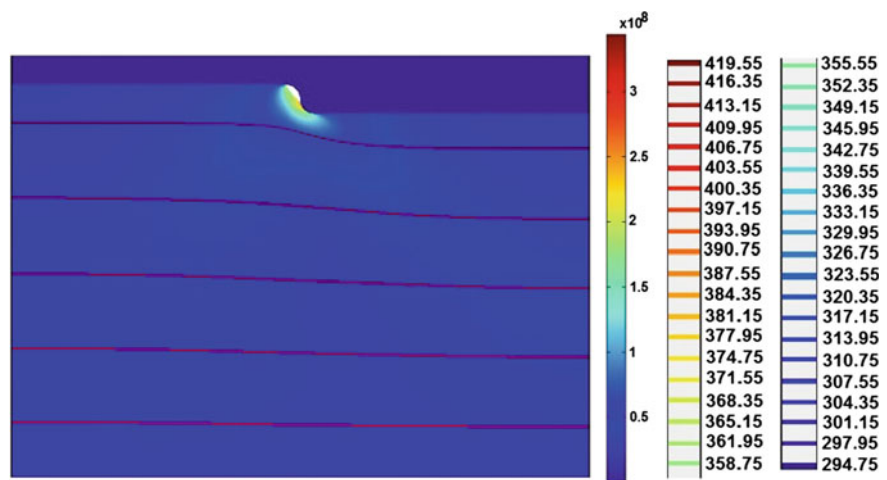


**Fig. 2.60** Von Mises stress distribution of deformed polycarbonate and temperature fields at  $9 \times 10^{-7}$  s after imprint step

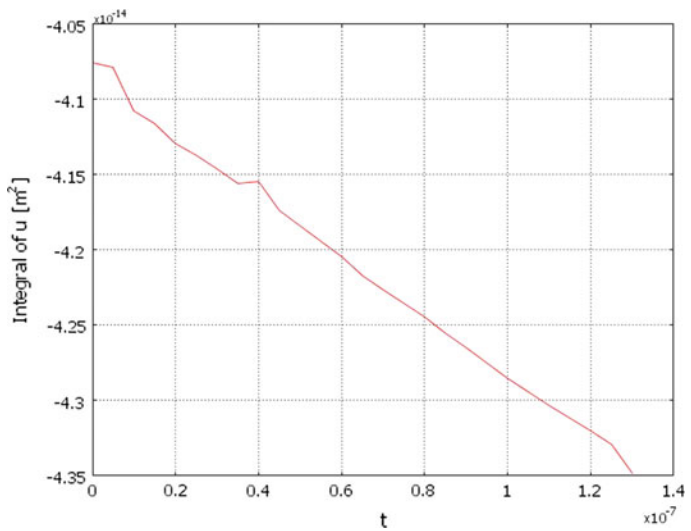


**Fig. 2.61** Integral displacement in x direction of contact edge in imprint step

3. Demolding step

When the mold was demolded and the temperature became equal to the ambient temperature 293 K, the plastic deformations took place in the polycarbonate. Their distribution is shown in Fig. 2.62. In this picture we can see how many times and in what areas they have exceeded the permissible limit of the yield.

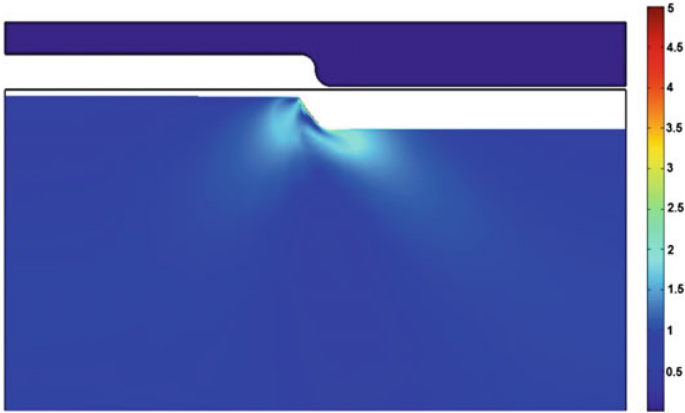


**Fig. 2.62** Areas of the permissible of yield

After demolding and cooling processes plastic deformation in the polycarbonate was observed. Model allows determine areas of the elastic and plastic deformations in the polycarbonate. The distribution of the ratio of Von Mises stress with yield strength of the polycarbonate is presented in Fig. 2.62. It shows that in some points Von Mises stress exceeds yield strength more than 5 times. Maximal ratio was observed in the corners of the formed structure.

In the demolding step the integral displacement module in x direction increases step by step (Fig. 2.63). It is so, because mold goes up discreetly.

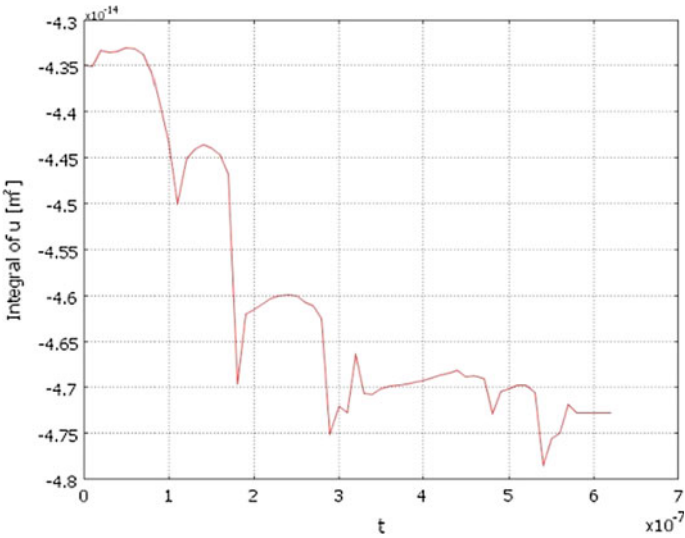


**Fig. 2.63** Integral displacement in x direction of contact edge in demolding step

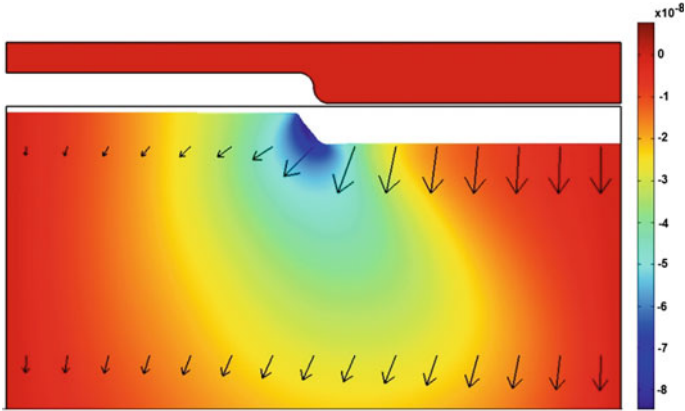


**Fig. 2.64** Horizontal direction displacement fields at  $7.1 \times 10^{-7}$  s, arrows represent total displacements in PC after demolding

As can be seen in Fig. 2.64, after the demolding, displacement fields in the x direction remain the biggest at the corner of the mold. The total displacement arrows are directed down, this means that during the demolding step the mold moves up and the polymer distributes into the empty cavities.

One of the most important quality parameters in hot imprint process is the percentage of filling ratio. It is defined as ratio of filled area and all area in microstructure.

As shown in Fig. 2.65, polycarbonate empty cavity decreases slowly at end of the heating step (mold moves to  $2 \times 10^{-7}$  m)—70%, then empty cavity rapidly decreases (when the mold moves to  $2.3 \times 10^{-7}$  m)—10%. At the end of imprint step empty cavity is reduced till 2% but in demolding step the empty cavity slightly increases and remains about 4%.

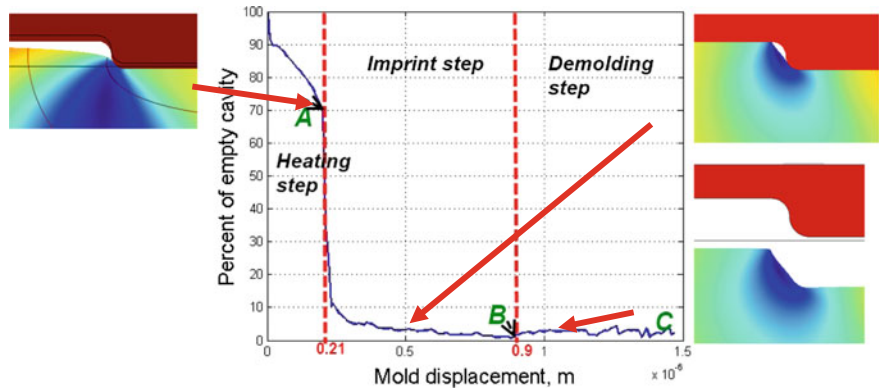


**Fig. 2.65** The dependence of non filling cavity from mold displacement

### 2.3.4 Finite Element Model Verification

The hot imprint experiment was performed on polycarbonate in order to check the validity of the results of imprint model simulation. A lamellar microstructure of 4  $\mu\text{m}$  period and 100 nm depth was used in hot imprint process (Fig. 2.66). It was imprinted into polycarbonate of 3 mm thickness at 148 °C temperature, 15 s time and 5 Atm pressure. This set (temperature, time and pressure) of parameters was experimentally determined by obtaining the replica of best quality. The experiments were made in these intervals: temperature—100 to 150 °C, time—5 to 15 s, pressure—1 to 5 Atm.

It is impossible experimentally to obtain the similar dependence as shown in the model results in Fig. 2.65. The initial microstructure (nickel mold) and obtained results were compared on the basis of AFM measurements.

Polycarbonate replication results are shown in Fig. 2.67. Figures 2.66 and 2.67 represent data, which were scanned with Matlab package and interpolated nearest neighbor method. The empty area of polycarbonate is about 10%.

This shows that the difference in comparison with simulation results is approximately 2.5 times. So we can say that the model is well made and is suitable for analysis and evaluation of the material behavior.

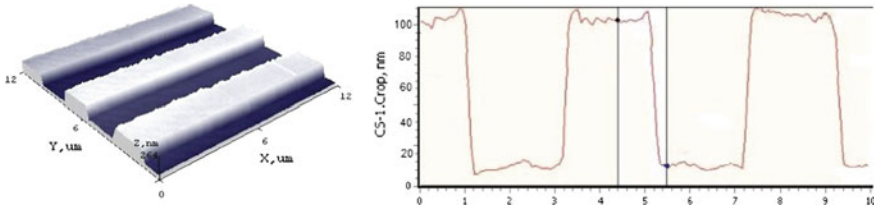


Fig. 2.66 Microstructure of nickel: *left* 3D surface; *right* profile

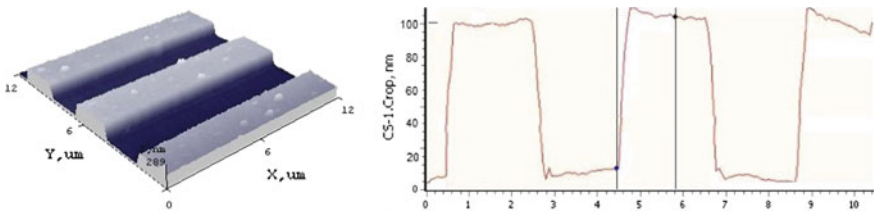


Fig. 2.67 Polycarbonate: *left* 3D surface; *right* profile from AFM

## References

1. Brown GC, Pryputniewicz RJ (1998) Holographic microscope for measuring displacements of vibrating microbeams using time-average electro-optic holography. *Opt Eng* 37:1398–1405
2. Pryputniewicz RJ, Furlong C, Brown GC, Pryputniewicz EJ (2001) Optical methodology for static and dynamic measurements of nanodisplacements. In: *Proceedings of international congress on experimental and applied mechanics in emerging technologies*, Portland, OR, pp 826–831
3. Pryputniewicz RJ, Stetson KA (1989) Measurement of vibration patterns using electro-optic holography. In: *Proceedings of SPIE*, vol 1162
4. Ostasevicius V, Palevicius A, Daugela A, Ragulskis M, Palevicius R (2004) Holographic imaging technique for characterization of MEMS switch dynamics. In: Varadan VK (ed) *Proceedings of SPIE*, vol 5389. Smart structures and materials 2004: smart electronics, MEMS, BioMEMS, and nanotechnology, pp 73–84
5. Ragulskis M, Palevicius A, Ragulskis L (2003) Plotting holographic interferograms for visualization of dynamic results from finite-element calculations. *Int J Numer Meth Eng* 56:1647–1659
6. Joroslavskij L (1987) Numerical processing of signals in optics and holography. 1987 M.: Radio i svjaz, 295 p
7. Palevičius A, Ragulskis M, Palevičius R (1998) Wave mechanical systems (theory, holographic interference). Caritas, Kaunas, 150 p
8. Palevičius A, Ragulskis M (1996) Holographic interference method for investigation of wave transport system. In: 2nd international conference on vibration measurement by laser techniques. Ancona, Italy, 1996, pp 21–27
9. Palevičius A, Ragulskis M (1998) The system of wave transportation and their holographic research. In: 3rd international conference on vibration measurement by laser techniques. Ancona, Italy, 1998, pp 125–128
10. Palevičius A, Ragulskis M, Tomasini E (1999) Vibramotor optimisation using laser holographic interferometry. In: *Proceedings of 17th international modal analysis conference*. Kissimme, USA SAE, 1999, pp 1012–1016
11. Gale MT (1997) Replication technology for holograms and diffractive optical elements. *J Imag Sci Technol* 41(3)
12. Lee B, Kwon M, Yoon J, Shin S (2000) Fabrication of polymeric large-core waveguides for optical interconnects using a rubber molding process. *IEEE Photon Technol Lett* 12:62–64
13. Siebel U, Hauffe R, Petermann K (2000) Crosstalk-enhanced polymer digital optical switch based on a W-shape. *IEEE Photon Technol Lett* 12:40–41
14. Oh M, Lee M, Lee H (1999) Polymeric waveguide polarization splitter with a buried birefringent polymer. *IEEE Photon Technol Lett* 11:1144–1146
15. Stutzmann N, Tervoort T, Bastiaansen C, Feldman K, Smith P (2000) Solid-state replication of relief structures in semicrystalline polymers. *Adv Mater* 12:557–562
16. Margelevičius J, Grigaliūnas V, Juknevičius V (1997) Forming specialities of micro-optical surfaces. In: *Materials science (Medziagotyra)*, ISSN 1392-1320, Kaunas: Technologija 1 (4):35–37
17. Meeder M, Zehnder R, Debruyne S, Faehnle OW (2003) In-process surface measurement of replication material during UV curing. FISBA Optik AG, Rorschacher Str. 268, 9016 St. Gallen, Switzerland
18. Schulz H, Scheer H-C, Hoffmann T, Sotomayor Torres CM, Pfeiffer K, Bleidiessel G, Grutzner G, Cardinaud C, Gaboriau F, Peignon M-C, Ahopelto J, Heidari B (2000) New polymer materials for nanoimprinting. *J Vac Sci Technol B* 18:1861–1865
19. Guobiene A, Cyziute B, Tamulevicius S, Grigaliunas V (2002) The evaluation of diffraction efficiency of optical periodic structures. *Mater Sci (Medziagotyra)* 8(3):235–239
20. van Renesse RL (1998) Optical document security, 2nd edn. TNO Institute of Applied Physics Stieltjesweg 1, Delft, The Netherlands. ISBN 0-89006-982-4, pp 29–55

21. Loewen EG, Popov E (1997) Diffraction gratings and applications. Marcel Dekker Inc., New York
22. Ferstl M (1998) OSA Tech Dig Ser 10:167–169
23. Martin C, Ressler L, Peyrade JP (2003) Study of PMMA recoveries on micrometric patterns replicated by nano-imprint lithography. *Phys E* 17:523–525
24. Baraldi LG (1994) Heißprägen in Polymeren für die Herstellung integriert-optischer Systemkomponenten. PhD Thesis, ETH, Zurich
25. Stoyanov S et al (2011) Modelling and optimization study on the fabrication of nano-structures using imprint forming process. *Eng Comput* 28(1):93–111
26. Juang YJ (2001) Polymer processing and rheological analysis near the glass transition temperature. Dissertation, 230 p
27. He Y, Fu JZ, Chen ZC (2007) Research on optimization of the hot embossing process. *J Micromech Microeng* 17:2420–2425
28. Lan S et al (2009) Experimental and numerical study on the viscoelastic property of polycarbonate near glass transition temperature for micro thermal imprint process. *J Mater Des* 30:3879–3884
29. Song Z et al (2008) Simulation study on stress and deformation of polymeric patterns during the demolding process in thermal imprint lithography. *J Vac Sci Technol B* 26(2):598–605
30. He Y, Fu JZ, Chen ZC (2008) Optimization of control parameters in micro hot embossing. *Microsyst Technol* 14:325–329
31. Liu C et al (2010) Deformation behavior of solid polymer during hot embossing process. *Microelectron Eng* 87:200–207
32. Jeong JH et al (2002) Flow behavior at the embossing stage of nanoimprint lithography. *Fibers Polym* 3(3):113–119
33. Yao DG, Vinayshankar LV, Byung K (2005) Study on squeezing flow during nonisothermal embossing of polymer microstructure. *J Polym Eng Sci* 45:652–660
34. Worgull M et al (2010) Hot embossing of high performance polymers. Design test integration and packaging of MEMS/MOEMS (DTIP), 5–7 May 2010, Seville, Spain, pp 272–277
35. Smidt LR, Carley JF (1975) Biaxial stretching of heat softened sheets: experiments and results. *Polym Eng Sci* 15(1):51–62
36. Day AJ et al (1993) Finite element modelling of polymer deformation process. In: ABAQUS user's conference, 1993, pp 151–163
37. Krishnaswamy P, Tuttle ME, Emery AF (1990) Finite element modelling of crack tip behavior in viscoelastic materials. Part 1: linear behavior. *Int J Numer Meth Eng* 30:371–387
38. Lin CR, Chen RH, Hung C (2002) The characterisation and finite element analysis of a polymer under hot pressing. *Int J Adv Manuf Technol* 20:230–235
39. Nicoli MA (2007) A thermo-mechanical finite element deformation theory or plasticity for amorphous polymers: application to micro-hot-embossing of poly(methyl methacrylate). PhD thesis, MIT
40. Kiew CM et al (2009) Finite element analysis of PMMA pattern formation during hot embossing process. In: IEEE/ASME international conference on advanced intelligent mechatronics, 14–19 July 2009. Suntec Convention and Exhibition Center, Singapore, p WB2.6
41. Kim NK, Kim KW, Sin HC (2008) Finite element analysis of low temperature nanoimprint lithography using a viscoelastic model. *Microelectron Eng* 85:1858–1865
42. Jin P et al (2009) Simulation and experimental study on recovery of polymer during hot embossing. *Jpn Soc Appl Phys: 06FH10-1-06FH10-4*
43. Hirai Y et al (2001) Study of the resist deformation in nanoimprint lithography. *J Vac Sci Technol B* 19(6):314–319
44. Young WB (2005) Analysis of the nanoimprint lithography with a viscous model. *Microelectron Eng* 77:405–411
45. Dupaix RB, Cash W (2009) Finite element modeling of polymer hot embossing using a Glass-Rubber finite strain constitutive model. *Polym Eng Sci* 49(3):531–543

46. Asaro RJ, Lubarda VA (2006) *Mechanics of solids and materials*. Cambridge University Press, New York, p 860
47. Haslach HW, Armstrong RW (2004) *Deformable bodies and their material behaviour*. Wiley, New York, p 560
48. Lemaitre J, Chaboche JL (1994) *Mechanics of solid materials*. Cambridge University Press, Cambridge, p 584
49. De Souza Neto EA, Peric D, Owen DRJ (2008) *Computational methods for plasticity: theory and applications*. Wiley, New York, 791 p
50. Lemaitre J, Chaboche JL (1990) *Mechanics of solid materials*. Cambridge University Press, Cambridge
51. Jirasek M, Bažant ZP (2002) *Inelastic analysis of structures*. Wiley, New York, 734 p
52. Rivera A (2007) *Non-linear finite element method simulation and modeling of the cold and hot rolling process*. PhD thesis
53. Crisfield MA (2001) *Non-linear finite element analysis of solids and structures*, vol 1. Wiley, Chichester, 345 p
54. Pennec F et al (2007) Verification of contact modeling with Comsol Multiphysics software. Paper presented at: EUROSIM: Federation of European Simulation Societies, Slovenia
55. Wriggers P (2006) *Computational contact mechanics*. Springer, Berlin, 518 p
56. Show MT, MacKnight WJ (2005) *Introduction to polymer viscoelasticity*, 1st edn. Wiley, Hoboken, 316 p
57. Reiter J, Pierer R (2005) Thermo-mechanical simulation of a laboratory test to determine mechanical properties of steel near the solidus temperature. In: Excerpt from the proceedings of the COMSOL Multiphysics user's conference. Frankfurt

Biomechanical Microsystems

Design, Processing and Applications

Ostaševičius, V.; Janusas, G.; Palevicius, A.; Gaidys, R.;

Jurenas, V.

2017, X, 282 p. 266 illus., 151 illus. in color., Hardcover

ISBN: 978-3-319-54848-7